COUNTER-FLOW IONIC WIND FOR HEAT TRANSFER ENHANCEMENT

A Thesis

Submitted to the Graduate School

of the University of Notre Dame

in Partial Fulfillment of the Requirements

for the Degree of

Master of Science in Mechanical Engineering

by

Sajanish M. Balagopal

_____

Dr. David Go, Director

Graduate Program in Aerospace and Mechanical Engineering

Notre Dame, Indiana

July 2011

COUNTER-FLOW IONIC WIND FOR HEAT TRANSFER ENHANCEMENT

Abstract

by

Sajanish M. Balagopal

The increasing complexity of electronic devices and components challenges conventional cooling techniques. For continued development in the electronics field, innovative cooling techniques are required. This thesis examines heat transfer enhancement of a heated plate experiencing low-velocity forced convection. A wire-to-rod corona discharge electrode configuration was used to generate a counter-flow ionic wind so as to direct the bulk gas flow in such a manner as to induce hot spot cooling. Particle image velocimetry (PIV) studies were conducted to profile the interaction between the bulk flow and counter-flow ionic wind and show how the hydrodynamic interactions result in a downward flow towards the heated surface and characteristic recirculation zones. This impingement-like effect enhanced the convection cooling of the heated plate, reducing the temperature by as much as 5 K. Convection coefficient was enhanced by up to 36% in the heat transfer experiments. In the PIV experiments,

seeding particles were used to obtain the fluid flow profile. As corona discharge creates a charged environment, seeding particles may get charged, and this may result in deviation from fluid flow due to Coulombic forces on the particles. To ensure the fidelity of the PIV results in these experiments, a simplified particle tracking analysis was conducted, solving the modified Basset-Boussinesq-Oseen (BBO) equation for particle motion and including charging and electric field effects to simulate the effects of corona discharge. The results obtained from these simulations were used to affirm the validity of the PIV results.

Dedicated to my mother and some teachers/faculties who took more than a passing interest in my life

CONTENTS

Tables v

Figures vi

List of Notations ix

Acknowledgments xiii

Chapter 1: Introduction 1
1.1 Overview 1
1.2 Electronic Cooling 1
1.3 Ionic Wind for Hot Spot Cooling 5
1.3.1 Ionic Wind Generation 5
1.3.2 Counter-flow Ionic Wind for Hot Spot Cooling 6
1.4 Research Objectives 8

Chapter 2: Corona Discharge and Heat Transfer 9
2.1 Overview 9
2.2 Corona Discharge Characteristics 9
2.2.1 Governing Equations 12
2.3 Ionic Wind in Flow Control and Heat Transfer 14

Chapter 3: Heat Transfer and Flow Visualization 19
3.1 Overview 19
3.2 Experimental Setup 19
3.3 Experimental Procedure 23
3.4 Results 24
3.4.1 Visualization 25
A. PIV Background 25
B. PIV Results 27
3.4.2 Heat Transfer 32

Chapter 4: Particle Tracking 45
4.1 Overview 45
4.2 Background 46
4.3 Model 50
A. Particle Force Balance 50
B. Electric Field 52
C. Charging and Tracking 54
4.4 Results 57

Chapter 5: Conclusion 64
5.1 Overview 64
5.2 Conclusion 64
5.3 Future Work 65

Bibliography 67

Appendix A: Particle Tracking Code 72

Appendix B: Additional Bulk Flow Velocity Information 75

TABLES

TABLE 3.1: FINAL STEADY STATE TEMPERATURES OF THE HEATED PLATE AT EACH THERMOCOUPLE LOCATION FOR THE CASE OF BULK FLOW ONLY AND BULK FLOW WITH IONIC WIND. BULK FLOW SPEED IS 1.2 m/s. IONIC CURRENT IS 40 μA 34

TABLE 3.2: FINAL STEADY STATE TEMPERATURES OF THE HEATED PLATE AT EACH THERMOCOUPLE LOCATION FOR THE CASE OF BULK FLOW ONLY AND BULK FLOW WITH IONIC WIND. BULK FLOW SPEED IS 1.7 m/s. IONIC CURRENT IS 40 μA 35

TABLE 3.3: FINAL STEADY STATE TEMPERATURES OF THE HEATED PLATE AT EACH THERMOCOUPLE LOCATION FOR THE CASE OF BULK FLOW ONLY AND BULK FLOW WITH IONIC WIND. BULK FLOW SPEED IS 1.2 m/s. IONIC CURRENT IS 20 μA 35

TABLE 3.4: FINAL STEADY STATE TEMPERATURES OF THE HEATED PLATE AT EACH THERMOCOUPLE LOCATION FOR THE CASE OF BULK FLOW ONLY AND BULK FLOW WITH IONIC WIND. BULK FLOW SPEED IS 1.7 m/s. IONIC CURRENT IS 20 μA 35

TABLE 4.1: VALUES FOR IMPORTANT PARAMETERS USED IN THE SIMULATION 55

FIGURES

Figure 1-1 Advertisement of a popular portable consumer device. Advertisement taglines show the market demands in the consumer electronic industry. Images taken from apple.com (iPad is a trademark of Apple Inc.). 2

Figure 1-2 Conduction cooling through usage of a heat frame on a printed circuit board 4

Figure 1-3 A positive corona discharge in a wire-to-cylinder geometry. 6

Figure 1-4 Counter-flow ionic wind using a corona generated by a wire-cylinder electrode combination (Not to scale). 7

Figure 3-1 (a) Photograph and (b) schematic (side view) showing the experimental flow channel and electrode positions. The heaters were placed in the gap shown under the Teflon sheet. For heat transfer measurements, thermocouples were placed just under the Teflon sheet, but above the heaters. The PIV laser illuminated the flow from the top, aligned with the midline of the experimental flow channel, and the PIV camera recorded images normal to laser sheet (from the perspective of the reader).....20

Figure 3-2 Positive corona generated in the experimental flow channel using a wire-cylinder electrode geometry. A high voltage was applied at the corona electrode and collecting electrode was at ground.....21

Figure 3-3 Schematic showing electrode-electrode separation distance and thermocouple positions. Thermocouple locations are indicated by dots numbered 1-4. 22

Figure 3-4 Basic schematic of PIV technique. 25

Figure 3-5 Vortex shedding observed in the flow channel in the absence of ionic wind. Red dot indicates the collecting electrode.....28

Figure 3-6 PIV images for the case of 1.2 m/s bulk velocity and two corona currents, 20 μA and 40 μA. The larger yellow dot indicates the collecting electrode, and the smaller yellow dot indicates the corona electrode. The bulk flow is from right to left. Distance scales in mm are attached to each plot for reference. 31

Figure 3-7 PIV images for the case of 1.7 m/s bulk velocity and two corona currents, 20 μA and 40 μA. The larger yellow dot indicates the collecting electrode, and the smaller yellow dot indicates the corona electrode. The bulk flow is from right to left. Distance scales in mm are attached to each plot for reference. 32

Figure 3-8 Steady state temperature reduction due to counter-flow ionic wind as a function of location corresponding to the four thermocouple locations as noted in the numbered boxes. The larger red dot indicates the collecting electrode, and the smaller red dot indicates the corona electrode, whose center was located at x = 0. 34

Figure 3-9 Heat transfer coefficients at each of the thermocouple locations for the case of 40 μA and 1.2 m/s. 40

Figure 3-10 Heat transfer coefficients at each of the thermocouple locations for the case of 40 μA and 1.7 m/s. 41

Figure 3-11 Heat transfer coefficients at each of the thermocouple locations for the case of 20 μA and 1.7 m/s. 41

Figure 3-12 Heat transfer coefficients at each of the thermocouple locations for the case of 20 μA and 1.2 m/s. 42

Figure 3-13 Heat transfer coefficient enhancement shown for all cases. Thermocouple locations are indicated in the numbered boxes [refer Fig. 3-3]. The larger red dot indicates the collecting electrode, and the smaller red dot indicates the corona electrode, whose center was located at x = 0. 44

Figure 4-1 Electric field lines near the particle (a)When the particle has zero charges (b) After reaching saturation charge. 47

Figure 4-2 Mesh used for solving the electric field. Higher mesh density is used near the electrodes. 57

Figure 4-3 Electric field map obtained from COMSOL for the wire-electrode geometry corona.....58

Figure 4-4 Electric field along x-axis. 59

Figure 4-5 Charge accumulation on a seeding particle in a corona discharge environment as a function of time for an initial position immediately adjacent to the corona electrode. 61

Figure 4-6 Deviation in the x and y velocities of the particle from the corresponding bulk fluid velocities. 62

Figure 4-7 Particle trajectory of the seeding particle. 63

LIST OF NOTATIONS

A	cross sectional area
a	particle radius
$\overline{c_i}$	mean ion thermal speed
D	diffusion coefficient
d_p	particle diameter
D_h	hydraulic diameter
e	elementary charge
$\vec{E}$	electric field
E_c	breakdown electric field strength of air
E_0	electric field at corona electrode surface
$\vec{F}_E$	electrohydrodynamics force
F_{cf}	field charging factor
F_i	external forces
g	gravity
h	height of experimental flow channel (between inside edges)
h_{bulk}	convection coefficient due to bulk flow
h_{ionic}	convection coefficient due to ionic flow
h_{total}	convection coefficient
I	current
$\vec{j}$	current density
k	Boltzmann's constant

K_E	electrostatic constant
k_f	thermal conductivity of medium
Kn	Knudsen number
l	length of heated plate
L_e	corona electrode length
n	number of charges on particle
N	ion density
n_d	number of charges by diffusion charging
N_{EHD}	electrohydrodynamic number
Nu	Nusselt number
Nu_{free}	Nusselt number for free convection
p	amount of charge
P	perimeter
P_p	local fluid pressure
P_{in}	power input to heaters
q	space charge density
q''	heat flux
R	total resistance of heaters
R_1, R_2	resistance of each heater
R_i	radius of the ionization zone
R_0	wire radius
Ra_c	critical Rayleigh number
Ra_L	Rayleigh number for characteristic length

Re_{Dh}	Reynolds number based on hydraulic diameter
Re_L	Reynolds number based on experimental flow channel length
S_n	ion source term
t	time
T	temperature of medium
T_f	film temperature
T_{bf}	temperature of bulk flow
T_h	temperature of heated plate
T_{sur}	temperature of experimental flow channel surface
U	bulk velocity in experimental flow channel
$\vec{u}$	fluid velocity
U_p	particle velocity
V	voltage
V_0	corona onset voltage
w	width of heated plate
x_{fd}	hydrodynamic entry length

GREEK SYMBOLS

α_{td}	thermal diffusivity of fluid
β_{te}	thermal coefficient of expansion of fluid
μ_E	ion mobility
ε	dielectric permittivity of fluid
ε_e	emissivity of heated plate

ε_0	dielectric permittivity of free space
ε_p	dielectric permittivity of particle
ε_r	relative permittivity
λ_i	mean free path of ions
ρ	mass density of medium
ρ_f	fluid density
ρ_p	mass density of particle
μ	dynamic viscosity
σ	Stefan-Boltzmann constant
ν	kinematic viscosity of fluid

ACKNOWLEDGMENTS

I would like to thank my advisor, Dr. David Go, for his patience, input and direction, all throughout my graduate studies. I am grateful to all the personnel of Small Scale laboratory, especially Rakshit Tirumala, for their help and support. The courses by Dr. Patrick Dunn and Dr. Scott Morris were very integral to my work and I would like to thank them and other faculties for the technical knowledge and expertise I received in courses at Notre Dame. This work would not have been possible without the help I obtained from a variety of people in furthering my educational pursuits from my primary school days.

CHAPTER 1:

INTRODUCTION

1.1 Overview

Cooling of electronic devices is an active area of research in the heat transfer community. This chapter discusses the field of electronic devices, which needs innovative techniques in heat transfer enhancement for continued development. The consumer portable electronic market is a growing area of interest to the industry, which brings some challenges in cooling requirements. Ionic wind-enhanced cooling can be a niche player in this area. This work therefore explores counter-flow for use in hot spot cooling.

1.2 Electronic Cooling

Electronics industry resembles the statement "change is the only constant”. Due to increasing processing speeds and continued miniaturization, cooling of electronic devices has always been an ongoing and challenging field for the heat transfer community. Heat removal from electronic devices plays a major role in the reliability of the device. Since electronic components do not involve moving parts, the emphasis for continued reliability is on operating temperature. The accurate performance and functioning of electronic devices is heavily dependent on the temperature. Thermo-

mechanical stresses that may result from high temperatures of chips boarded on the circuit boards are also a major factor in reliability. A good thermal packaging hence makes use of an optimum combination of various heat transfer modes, phase change processes, and heat transfer enhancement techniques [1]. Due to access and low cost, there has been a preference for air cooling especially in computing devices. So methods to increase air cooling rate continues to be a major area of research [2].

Figure 1-1 Advertisement of a popular portable consumer device. Advertisement taglines show the market demands in the consumer electronic industry. Images taken from apple.com (iPad is a trademark of Apple Inc.).

Recently, several of the high selling consumer products in tablet computers, laptops, mp3 players, storage drives and other portable devices have put an emphasis

on being thinner, faster and lighter. Fig. 1-1 shows the tagline of a popular portable electronic device. The result has been higher and higher power densities and increased need for innovative cooling techniques. A representative chip packaging in such electronic devices will be as follows. A number of chips are mounted closely through a low resistance bond on a substrate, called a multi-chip module. A single chip module on the other hand will only have a single chip on the substrate. Multi-chip modules have enhanced performance due to shortened wire lengths and also have reduced costs due to economical chip packaging. The substrate is typically made of ceramic or plastic. Usually an alloy lead frame is used in between the silicon chip and the substrate. This is to avoid the thermal stresses that may result from the hugely different coefficients of expansion of the silicon and the substrate. The alloy has an expansion coefficient that is closer to that of the silicon. These modules are usually enclosed in protective covers with pins extending from it. These pins connect the chip package to the printed circuit boards (PCBs), which facilitates communication between various chips. These PCBs are connected to the motherboard which allows interconnection between various circuit boards. At the chip level, the emphasis for dissipating heat is through conduction. Hence high-conductivity bonding materials are regularly made use of. The PCBs are usually cooled by convection with air as the medium. For some applications, heat dissipation from the PCBs also makes use of conduction cooling [3]. This may be necessary to reduce hot spot areas in the inner regions of the PCB. In this case, the PCBs are usually mounted on a high conductive heat frame which helps dissipate the heat towards the edges, which usually contain cold plates as shown in Fig. 1-2 [3]. This heat frame is often

implemented through a thicker copper layer surrounding the bottom of the chip on the surface of the PCB that extends towards the edges. Assuming that the electronic components (chips in Fig. 1-2) are all equally spaced and generate equal amounts of heat, the temperature of the PCB will be as shown in the figure. Higher energy chips in the inner regions of PCB may thus cause further localized increases in temperatures, thus necessitating a need for hot spot cooling.

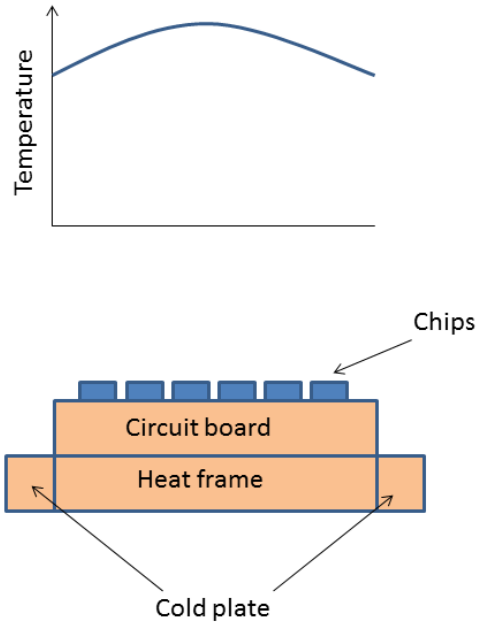

Figure 1-2 Conduction cooling through usage of a heat frame on a printed circuit board.

As consumer expectations have risen, so has the need for cooling. This is especially so in the case of portable electronic devices. The device skin temperature, acoustic noise from the device, the battery life and the device size are important parameters that define consumer experience and their acceptance among the consumers. Most of these parameters bring further challenges to the field of electronics

cooling like higher heat load, reduced surface area for heat transfer and a restriction on methods that can be used in devices for cooling purposes. Hence it is essential to look at innovative methods of cooling. An ionic wind, which is generated by corona discharge, is such a method that can be used in heat transfer enhancement applications. Ionic wind cooling has some advantages that are suited for application in electronic devices. It has low power consumption and generates very little acoustic noise. It requires no moving parts to operate and therefore it has low maintenance requirements. Due to the fast response time of corona discharge to applied voltage, the ionic wind velocity magnitude can be varied in a rapid manner.

1.3 Ionic Wind for Hot Spot Cooling

Ionic wind can be used to generate or enhance forced convection heat transfer by appropriate selection of the electrode geometry and location. Due to the possibility of smaller scaling than conventional devices like fan, it can be tailored in such a way as to induce hot spot cooling in small portable devices.

1.3.1 Ionic Wind Generation

A corona discharge occurs when a high potential difference is applied between two electrodes, one of them with high-curvature geometry. Due to the sharp geometry of one of the electrodes, known as the corona electrode, field lines converge and cause a highly localized increase in the electric field near corona electrode. When this localized high field exceeds the breakdown strength of the medium (usually air), ionization of the medium occurs, in a confined region known as ionization zone as shown in the Fig. 1-3.

During this discharge, the ions generated near the corona electrode move towards the oppositely charged electrode under the influence of the electric field and transfer momentum to the neutral air molecules on the way. This can introduce a low velocity bulk gas motion known as an ionic wind, which can then be used to generate or enhance forced convection heat transfer. Because an ionic wind can modulate and distort a pre-existing bulk flow, a controlled convection enhancement can be achieved by varying the magnitude and direction of the electric field.

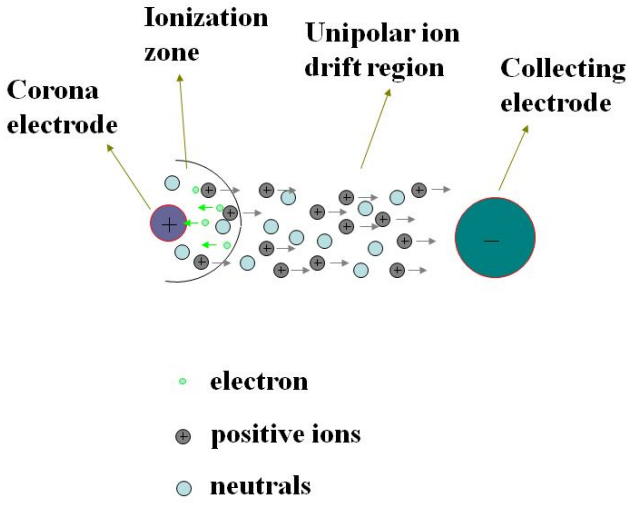

Figure 1-3 A positive corona discharge in a wire-to-cylinder geometry.

1.3.2 Counter-flow Ionic Wind for Hot Spot Cooling

Ionic winds can be generated in the direction of an already existing flow or in opposition to it. It can be said in a general way that co-flow ionic winds are in the direction of the bulk flow and counter-flow ionic winds are those opposing the bulk flow. Depending on the polarity of the corona electrode, the discharge is known as

positive corona or negative corona. Higher velocity ionic wind can be generated using a positive corona discharge for the same conditions [4]. This is attributed to the nature of the discharge mechanism (positive streamers) and drifting charge carriers (larger positive ions). A counter-flow ionic wind can be used to modulate a low velocity bulk flow as shown in Fig. 1-4, which shows an ionic wind generated by a positive corona, wire–cylinder electrode configuration. The bulk flow is from right to left. The ionic wind generated by the corona discharge is from left to right. Depending on the relative magnitude of the ionic velocity compared to the bulk flow, the interaction between the two velocities is expected to result in the bulk flow diverting towards the walls, accelerating near the wall boundaries and/or impinging on the walls. The region at the boundaries where the bulk flow accelerates and/or impinges can be used as a hot spot cooling region.

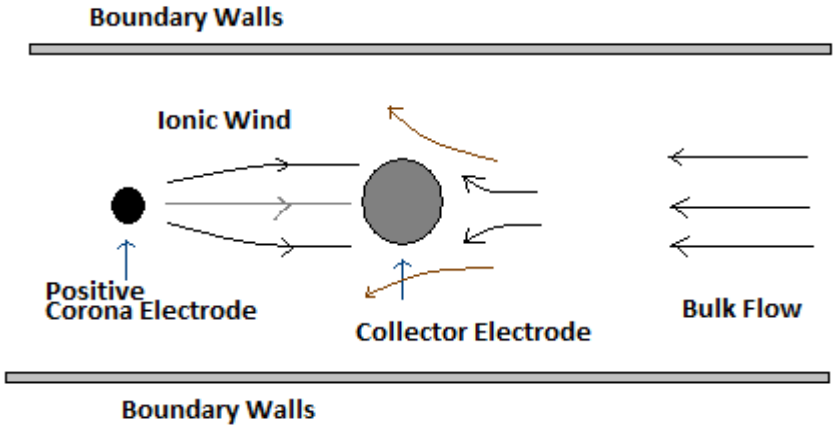

Figure 1-4 Counter-flow ionic wind using a corona generated by a wire-cylinder electrode combination (Not to scale).

1.4 Research Objectives

The objective of this work was to study the influence of counter-flow ionic wind on the heat transfer rate from a heated plate. The parameters varied were the ionic wind velocity and the bulk flow velocity. Temperature measurements were taken to study the ionic wind enhancement of the convection heat transfer coefficient. Visualization methods like particle image velocimetry (PIV) and smoke visualization were used for revealing the fluid flow structures that lead to increased cooling. The visualization results needed to be validated as seeding particles are located in a high electric field region with significant number of charges. A simplified particle tracking analysis was conducted to add confidence to the PIV results.

In Chapter 2, the basics of corona discharges are discussed. The governing equations of corona discharge relating to electric field, current and force are outlined. A literature review of the use of ionic wind in heat transfer enhancement is also discussed. Chapter 3 presents the experimental method and results. The experimental setup is introduced, followed by a brief description of the PIV method. Visualization results and heat transfer results are presented next. In Chapter 4, the particle tracking method and results are described. Chapter 5 concludes this study and future work is suggested.

CHAPTER 2:

CORONA DISCHARGE AND HEAT TRANSFER

2.1 Overview

This chapter discusses the basic features of corona discharge. The governing equations in corona discharge are noted. The chapter closes with a discussion of application of ionic wind in heat transfer and a literature review of the same.

2.2 Corona Discharge Characteristics

Plasma is an electrically neutral medium of ionized gas, usually consisting of ions, electrons and neutral species. Low-temperature or cold plasmas are typically known as gas discharges, the other being high-temperature or thermal plasmas. Gas discharges are widely used in many applications like photocopiers, jet printers and electrostatic precipitators (ESPs) especially as an ion source. Cold plasmas are usually classified as non-equilibrium or non-local thermal equilibrium (LTE) discharges. Different species in the ionized region (ions, electrons, neutrals) are not at the same temperature. Usually electron temperature will be high compared to the heavier particles (ions, atoms, and molecules) in the gas. In most cases, the high electron temperature (high electron speed) helps in sustaining the discharge process through electron impact ionization and also in generating large number of chemically reactive species. Most of the energy given

to the discharge by the applied power source is used for production of energetic electrons [5]. These electrons are able to produce excited species through impact with the rest of the particles.

Corona discharge at atmospheric pressure is a low temperature, non-LTE, low-power consumption discharge. This has recently been the subject of a lot of scientific research due to some recent studies on ionic winds. In corona discharges, breakdown of the medium occurs only in the narrow ionization region. Hence this results in a partial discharge. Ions created in this region then travel through a low field *drift region* towards the low curvature, oppositely charged electrode known as the collecting electrode. Polarity of the drifting ions will be same as that of the corona electrode. In drift region, electric field is low and the electrons and ions are not able to accelerate sufficiently to produce more charge carriers on the way. If the high electric field in the ionization region is near the anode, then it is called a positive corona. Similarly, if the high electric field is near the cathode, then it is called a negative corona.

In a positive direct current (DC) corona, the resident electrons in the ionization region get accelerated due to the high electric field towards the corona electrode and eject electrons from neutral air molecules. The newly created electrons produce more ions and electrons, resulting in an avalanche. Secondary electrons in a positive corona are produced by photoionization occurring in the gas phase, resulting from photon emission during de-excitation. In a positive corona discharge in air, the ion composition includes $N_2^+, N_{4,}^+ O_2^+, O_4^+, CO^+, Ar^+, CO_2^+,$ and H_3O^+.

Similarly In a negative corona, resident electrons create the avalanche. However, sustaining ionization in a negative corona depends significantly on secondary emission from cathode through ion bombardment. Due to the nature of electron production from the surface of negative corona electrode, electrode material is more important in the case of negative coronas. For creating negative corona discharge, gases such as oxygen, water vapor and carbon dioxide that have high affinity for electrons are needed. For example, in gases with no affinity towards electrons, spark occurs instead of a corona discharge. Thus the gas medium is more important in the case of negative corona. The negative corona composition consists of O^-, O_2^-, O_3^- and CO_3^- ions with electrons. The effect of temperature on the mobility of these ions, and hence in a negative corona, is expected to be more, thereby causing a larger decrease in current than in the positive corona [6]. Negative coronas generate a higher ozone concentration than a positive corona for the same discharge conditions. This is due to the presence of a higher number of electrons in negative corona than a positive corona.

Current-voltage relationship during a corona discharge [7] is given by

$$I = CV(V - V_0), \tag{2.1}$$

where I is discharge current per unit wire length, V_0 is voltage at corona onset, C is a constant which depends on the geometry, material and electrode polarity. The current generated depends upon voltage supplied above the critical voltage, V_{cr}. The critical voltage corresponds to the minimum voltage required to create the critical electric field, which would result in an ionization zone near the corona electrode. The electrical current to the collecting electrode is provided by the drifting of unipolar ions or

electrons through the drift region. The space charge created by this acts as a resistor, and this limits the generated current (in ionization region) that is delivered to the electrode. This space charge also creates an electric field that opposes the applied electric field. This will cause the applied field value to change slightly.

2.2.1 Governing Equations

Applying suitable boundary conditions, the potential, *V* during a corona discharge can be related to space charge using Poisson's equation

$$\nabla^2 V = -\frac{q}{\varepsilon_0}, \tag{2.2}$$

where q is space charge density, and ε_0 is the dielectric permittivity of free space (8.854 x 10^{-12} F/m). Electric field, $\vec{E}$ is related to the electric potential by

$$\vec{E} = -\vec{\nabla} V , \tag{2.3}$$

The current density, $\vec{j}$ is

$$\vec{j} = \mu_E \vec{E} q + \vec{u} q - D\vec{\nabla} q , \tag{2.4}$$

The terms on the RHS represent the contribution to current due to electric drift, advection and diffusion, respectively, where $\vec{u}$ is the fluid velocity (m/s), μ_E is the ion mobility, and *D* is the diffusion coefficient of ions (m^2/s). Advection term can be neglected when $\vec{u}$ is much smaller than $\mu_E \times \vec{E}$ [8]. The current continuity equation in the drifting zone can be expressed as

$$\frac{\partial q}{\partial t} + \nabla \cdot j = S_n , \tag{2.5}$$

where S_n is the source term.

Electrohydrodynamics (EHD) refers to the study of interaction between the electric field and fluid flow in electrically charged medium. The EHD force in a fluid of dielectric permittivity ε, mass density ρ, and temperature T can be expressed as [9]

$$\vec{F}_E = q\vec{E} - \frac{1}{2}E^2\nabla\varepsilon + \frac{1}{2}\nabla\left[E^2\left(\frac{\partial\varepsilon}{\partial\rho}\right)_T \rho\right], \tag{2.6}$$

The first term on the right hand side (RHS) is the Coulombic force resulting from free charges within the fluid. The second and third term represent the dielectrophoretic force and the electrostrictive force respectively. The second term and third term are important in phase change processes where the permittivity variation will be high at the liquid-vapor interface. For the third term, the higher density variation at the interface in a phase change process contributes substantially to the EHD force [10]. For air, the permittivity variation is negligible, and hence the dominant term in Eq. (2.6) is the Coulomb force term.

Including the EHD force term, the Navier-Stokes equation for a moving fluid becomes

$$\vec{\nabla}\cdot\left(\rho\vec{u}\vec{u}\right) = \mu\nabla^2\vec{u} - \vec{\nabla}P_p + \rho\vec{g} + \vec{F}_E \ , \tag{2.7}$$

where μ is dynamic viscosity (N-s/m^2), $\vec{u}$ is the fluid velocity (m/s), P_p is the local fluid pressure and $\vec{g}$ is gravity (m/s^2). The first, second, third and the fourth term represents the viscosity, pressure gradient in the fluid, gravity force per unit volume and EHD force term, respectively. Viscous effects are usually negligible if domain being considered is far from the boundaries. The continuity equation for the fluid is obtained as

$$\nabla \cdot (\rho \vec{u}) = 0 \ , \tag{2.8}$$

The effect of ionic wind on the fluid flow can be characterized by the dimensionless electrohydrodynamic number, N_{EHD} [11] given by

$$N_{EHD} = \frac{I}{L_e \rho \mu_E u^2} \ , \tag{2.9}$$

where I is the time averaged corona current, L_e is corona electrode length and u is bulk flow velocity. N_{EHD} is a measure of the ratio of the corona-discharge induced force to that due to the inertia of the gas. Electric body force per unit volume is given by $\frac{I}{\mu_E}$. Dividing this by inertial body force ρu^2 and non-dimensionalising that ratio by multiplying with $\frac{1}{L_e}$ gives the N_{EHD} number. A very high N_{EHD} is an indication that the air flow is considerably affected by the ionic wind [11].

2.3 Ionic Wind in Flow Control and Heat Transfer

Heat transfer enhancement methods can be broadly categorized into passive and active techniques. Fins, surface modifications, and fluid additives are part of the category of passive techniques. Active techniques require an input power for their desired effect. Ionic wind is an active technique that is used for heat transfer enhancement. The use of ionic wind has been studied in other applications like drag reduction [12–17] and flame kinetics [18-19].

There are various advantages of the ionic wind method in applications where a low current, high voltage power supply is available. These include direct conversion of

electric energy to kinetic energy without any moving parts, no vibration, no lubrication requirements, low power consumption, simple sturdy construction and little to no acoustic signature. However the efficiency of electrokinetic conversion is usually low at about 1% [20]. However efficiencies of upto 7.5 % have been reported in literature [21].

A quantitative explanation of the ionic wind was provided by Chattock in 1899 [22]. Robinson [20] investigated the mechanism of gas movement in ionic wind and found that gas velocity is proportional to current and is a linear function of voltage. It was also noted from experiments that corona current was basically independent of gas velocity, investigating up to a velocity of 15 m/s. Using a needle point as corona electrode and a wire screen as the collecting electrode, increasing the gas velocity to a range of 12-15 m/s for various applied voltages, yielded the same corona current. Marco et al. [23] studied the use of this technique as early as 1963. They used a corona wire electrode to impinge the ionic wind on a heated collector plate, and obtained an enhancement of average heat transfer coefficient up to five times over that for natural convection. Momentum integral analysis showed good agreement with experimental results. It was observed that the non-dimensionalised temperature profiles at lower ionic wind velocities resembled that at higher bulk velocities with no corona current. Owsenek et al. [9] studied EHD heat transfer enhancement for natural convection with wire electrodes above a heated horizontal collecting electrode and verified them with numerical studies. An impingement flow was created for the case of single corona electrode, and enhancements by factors up to 8.5 were achieved. For multiple wire electrodes, impingement regions and recirculation zones were observed. They also

observed high heat transfer coefficients at the impingement regions and reduced heat transfer at recirculation zones. Franke [24] investigated the effect of vortices induced by corona discharge generated using alternate high voltage and ground potential parallel wires placed vertically on the surface of a phenolic plate. Interferometer studies revealed the formation of counter-rotating vortices near the surface of the plate. Pour [25] et al. conducted studies on convective heat transfer enhancement in a duct using corona wind for various Reynolds numbers (*Re*) for both forced and natural convection. It was noted that at lower *Re*, there is a smaller difference in enhancement ratio over various voltages due to the EHD effects becoming saturated. By suitable arrangement of electrodes, secondary flows were created in recirculation zones or dead zones, and this was verified with smoke visualization. Yehia et al. [26] conducted experimental investigations to determine the effect of magnitude and direction of the air flow rate on characteristics of the corona discharge. The corona onset voltage was observed to be independent of the air flow magnitude and direction for any polarity of the corona discharge (positive, negative or alternating current). Current-voltage characteristics were observed to depend on the air flow rate magnitude. Corona current showed an increase for increasing air flow rate up to 2 l/min. for positive coronas and 4 l/min. for negative and alternating current coronas. After this increase, the current decreased with further increase of air flow rate. This was observed for both parallel and normal (to the electrodes) air flow direction. Kalman et al. [27] investigated heat transfer enhancement with a wire corona electrode confined by two inclined wing (collecting) electrodes. They concluded that the conversion efficiency of an electrical power to mechanical energy is

higher in a positive corona than in negative corona. They observed that the ionic wind velocity was consistently higher for the positive corona compared to the negative corona for the same voltage applied, reaching a 20 % increase at the peak velocity. This was inspite of the higher current values observed for negative corona and explained it as due to the higher mobility of negative ions. Mahmoudi et al. [28] studied the effect of ionic wind generated by a blade edge corona electrode on free convection heat transfer from a heated horizontal cylinder. Numerical simulations were conducted to find flow patterns, and the enhancement was stronger at lower Rayleigh, *Ra* numbers. A recirculation zone appeared at a specific corona voltage and increased in intensity till breakdown voltage (with corona current increase), causing decrease in local cooling near the recirculation region. Numerical studies revealed a larger space charge concentration near the blade edge electrode. Numerical studies and experiments revealed a decreasing enhancement of heat transfer with *Ra* number. Higher temperatures at the cylinder (collecting electrode) were assumed to have caused the decrease in corona current at the same applied voltage. A probable reason was mentioned as the decrease of ion mobility with increase of surface temperature of the cylinder. Molki et al. [29] studied the application of ionic wind for heat transfer enhancement in the developing region of a circular tube. The co-axial electrode arrangement where the corona electrode was along the axis of the tube generated a radial ionic wind normal to the flow, generating local and average heat transfer coefficient enhancement of 14-23% and 6-8% respectively. Yabe et al. [30] studied corona wind generated by a wire corona anode and a plate cathode. It was

experimentally clarified that there are very few electrons in the whole space and positive ions and neutrals predominate except in the extremely narrow region close to the wire anode. Numerical calculations based on these findings showed a good match with experimental results of pressure and potential. Earlier works by Go et al. [31-32] used ionic winds to promote hot spot cooling in external flow. The ionic wind was used in the presence of an external flat plate flow to modulate the boundary layer where heat transfer enhancement was desired. The local heat transfer coefficient was observed to be enhanced by up to 200% over that obtained from the bulk flow alone. Literature reviews on ionic wind based enhancement of heat transfer can be found in the works by Molki [29], Allen et al. [33], Ohadi et al. [10], and Laohalertdecha et al. [34].

CHAPTER 3:

HEAT TRANSFER AND FLOW VISUALIZATION

3.1 Overview

This chapter focuses on the experimental investigation of enhancement in heat transfer due to the presence of ionic wind and visualization of the fluid flow. Low velocity bulk flow was modulated with the usage of ionic wind. The parameters varied for the study were the magnitudes of ionic wind and bulk flow velocities. Thermocouples were placed at four locations beneath the heated plate to record the temperature drop due to ionic wind. PIV and smoke visualization were conducted to understand the flow interactions due to ionic wind and bulk flow which resulted in increased heat transfer.

3.2 Experimental Setup

A schematic and a photograph of the corona discharge experiment are shown in Fig. 3-1. A miniature experimental flow channel was constructed, and consisted of a flow straightener at the experimental flow channel entrance and a fan operating in suction mode at the channel exit, which pulled the air through the straightener into the test section creating a bulk flow. The whole structure was made from electrically insulating plastic, and the length, width and height of the test section were 179 mm, 51

mm, and 19 mm respectively. For the experiment, the fan voltage (0-25 V E3631A, Agilent) was adjusted such that it provided two bulk flow speeds of approximately 1.2 ± 0.058 m/s and 1.7 ± 0.069 m/s.

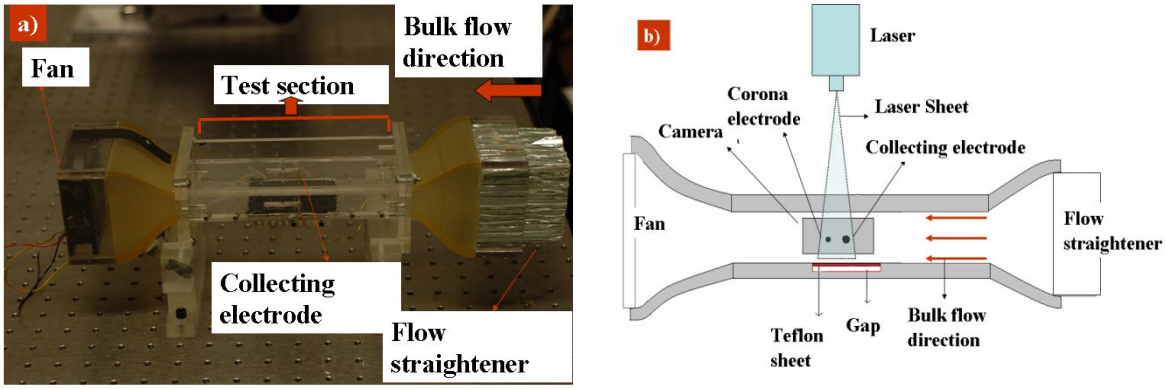

Figure 3-1 (a) Photograph and (b) schematic (side view) showing the experimental flow channel and electrode positions. The heaters were placed in the gap shown under the Teflon sheet. For heat transfer measurements, thermocouples were placed just under the Teflon sheet, but above the heaters. The PIV laser illuminated the flow from the top, aligned with the midline of the experimental flow channel, and the PIV camera recorded images normal to laser sheet (from the perspective of the reader).

A typical corona discharge generated for the experimental studies is shown in Fig. 3-2. The electrodes consisted of a 50 µm tungsten wire as the corona electrode and a 1.57 mm outer diameter copper cylinder as the collecting electrode. In order to generate a counter-flow ionic wind, the electrodes were placed with the corona wire downstream of the collecting electrode such that the discharge was in a direction opposite of the bulk flow. The electrodes were separated by a spacing of 4.7 mm (electrode edge-to-edge) as shown in Fig. 3-3. The power to the corona electrode was provided by a 0-10 kV DC high voltage power supply (Bertran Series 225). A positive DC

voltage ranging from 6.5-7.3 ± 0.012 kV was applied on the corona wire electrode, and the collecting electrode was maintained at ground. The corona current was measured with a picoammeter at the grounded electrode (Keithley 6485).

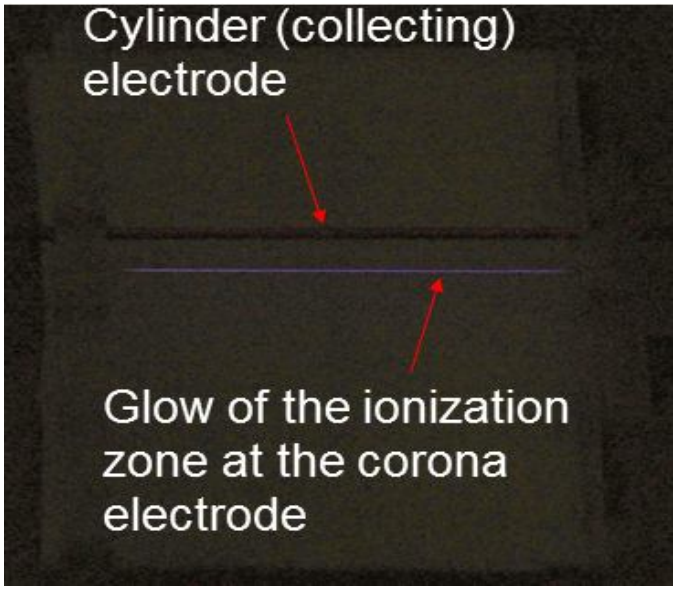

Figure 3-2 Positive corona generated in the experimental flow channel using a wire-cylinder electrode geometry. A high voltage was applied at the corona electrode and collecting electrode was at ground.

The PIV measurements were conducted using a FlowMaster Planar PIV system (LaVision Inc.). A 532 nm Nd:YAG laser with a pulse energy of 30 mJ (Solo II-30, New Wave Research) was used to provide light during exposure, and images were recorded using an Imager ProX 2M camera. For single frame images, a frequency rate of 30 fps was possible, and for PIV experiments, double frame/double exposure images were taken with the camera frequency rate at 14.7 fps. The timing between the two images (for each set of double frame image) was varied from 28-32 μs, depending upon the bulk velocity used. The experimental flow channel was kept in an optically transparent

box that was filled with seeding particles provided by incense sticks, and the seeding density was controlled by the burning time. Cross correlation analysis on the images was conducted using Davis 7 software with variable windows size (final size is 32 by 32 pixels) and 50% overlap.

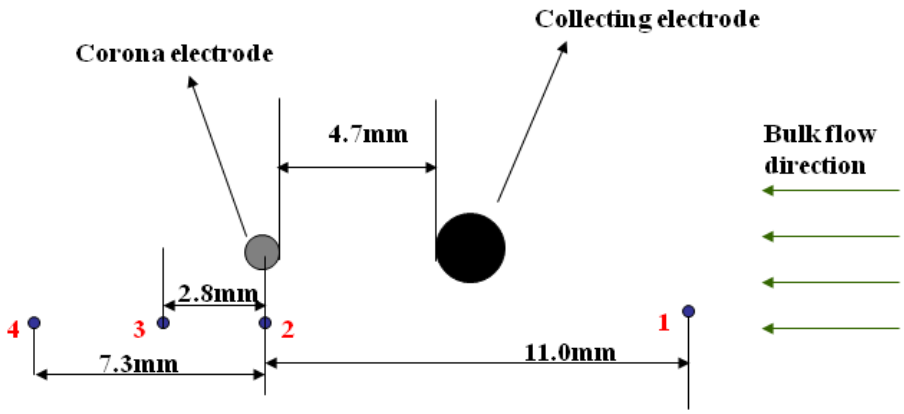

Figure 3-3 Schematic showing electrode-electrode separation distance and thermocouple positions. Thermocouple locations are indicated by dots numbered 1-4.

For heat transfer measurements, a Teflon sheet, 1 mm in thickness, was placed in a counter-sunk recess, flush with the surface of the bottom horizontal wall of the test section as shown in Fig. 3-1. It extended 31 mm upstream and 46 mm downstream of the collecting electrode. The Teflon sheet was placed such that any flow modification effected by the ionic wind will occur primarily within the length of the Teflon sheet, thus capturing the heat transfer enhancement of the ionic wind. K-type thermocouples (HSTC-TT-K, Omega Engineering) were used to measure the local temperature of the Teflon sheet and were placed just below the surface at four locations as shown in Fig. 3-3. The thermocouples were read using a K-type thermocouple thermometer (Omega

450 AKT). Two 2.5 cm by 5 cm film heaters (KHLV series, Omega Engineering) were placed at the bottom of the recess, and a thermally conductive putty (TIM-putty, Timtronics) was used to fill any space between the thermocouple, heater, and Teflon sheet to ensure good thermal contact. The Teflon sheet was painted with Krylon ultra flat black spray 1602 of known emissivity on the side exposed to air flow [35] in order to accurately calculate radiation. The two heaters were powered by a variable transformer power supply (Variac series, ISE Inc.) and operated so that a constant total heat of 2.3 ± 0.1096 W was delivered to the Teflon sheet.

3.3 Experimental Procedure

PIV experiments were initially run without ionic wind (no corona discharge) to determine the effect of the physical presence of the electrodes alone on the fluid flow. Following this, PIV was conducted over a series of combinations of corona currents (20 ± 0.02 μA and 40 ± 0.04 μA) and bulk fluid velocities (1.2 m/s and 1.7 m/s). Fan speeds were initially run much higher than these velocities to facilitate better seeding homogeneity in the experimental flow channel, and then reduced to their experimental values. Thirty images were taken for all experiment runs and the results presented herein were time-averaged across all the images.

The heat transfer experiments were conducted independently of the PIV studies to avoid precipitating the seeding particles. The heater and fan were set at their required settings for the heater power and experimental bulk flow velocity, respectively. After the temperatures measured by the thermocouples reached steady state values, a

corona discharge was activated. The temperatures were then measured until they reached steady state values.

3.4 Results

For the bulk flow speeds used, Reynolds numbers based on the hydraulic diameter, $Re_{Dh} = \frac{\rho u D_h}{\mu}$ were calculated where D_h is the hydraulic diameter of the flow channel. For the flow channel used in experiment, it was calculated as $D_h = \frac{4A}{P}$ where A is cross sectional area of the flow channel and P is the cross sectional perimeter of the flow channel. Re_{Dh} was obtained as 2118 and 3001 for bulk speeds of 1.2 m/s and 1.7 m/s respectively, which implies that the flow is in the transition region. However, direct visualization of the flow suggested that the flow was laminar for both cases. For laminar flow ($Re_{Dh} \leq 2300$), the expression for hydrodynamic entry length is given [36] by $\frac{x_{fd}}{D_h} \approx 0.05 Re_{Dh}$ where x_{fd} denotes hydrodynamic entry length. Calculating this for both Reynolds number, x_{fd} was obtained as 2.92 m and 4.15 m for Re_{Dh} numbers of 2118 and 3001 respectively. The entrance length for both velocities was greater than a meter, such that the flow was always in the developing region. As such, the corona electrodes were essentially in a free stream, laminar flow (the Reynolds numbers based on the length of the duct, Re_L were 13698 and 19406 for 1.2 m/s and 1.7 m/s, respectively). Even though there are charged species present in the fluid medium, the ratio of free charges to that of neutral molecules is around 10^{-10} [37]. Hence the changes in heat

transfer rate can be explained on the basis of fluid mechanics rather than due to changes in physical properties like thermal conductivity and viscosity [38].

3.4.1 Visualization

Smoke visualization and PIV were used to record the fluid structures and flow characteristics that explained the heat transfer results from a flow dynamics perspective.

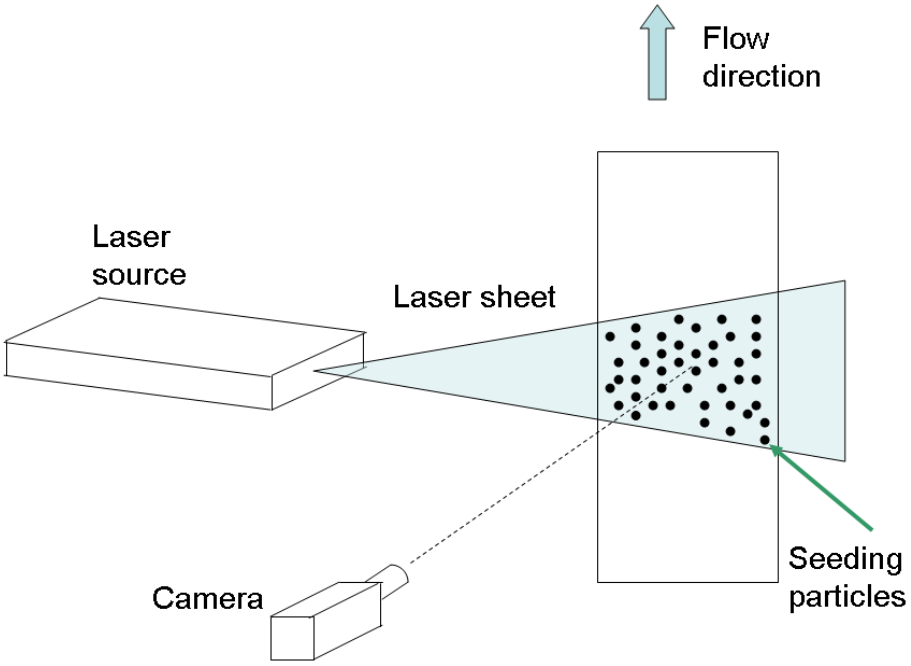

Figure 3-4 Basic schematic of PIV technique.

A. PIV Background

PIV is a visualization technique widely used in fluid studies for obtaining quantitative as well as qualitative information about the flow. PIV requires a transparent view to the flow of the fluid, which is also required to be a transparent medium. The fluid flow to be studied is seeded with small particles of the size of micrometers. A laser

source is used to illuminate the seeded flows in the region of interest. A camera which is synchronized with the laser source records the images and these images are then processed to get the flow field information. PIV provides instantaneous whole field flow velocity maps with high accuracy.

A thin light sheet (typically 0.5 mm to 2 mm thick) from the laser source is illuminated twice at the region of interest as shown in Fig. 3-4. Thus the positions of seeding particles in this narrow light sheet are captured by the camera. The illumination interval is determined based on the velocity of the flow to be captured. The images are either recorded as a single image exposed twice (single frame-double exposure) or as two single images (double frame-double exposure). These images are then subdivided into small subsections called interrogation windows (IW). As a rule of thumb, each IW should have around 7-12 particles for accurate velocity mapping. The displacement of the seeding particles in the IW is used along with time interval between the two exposures to obtain velocity of each particle. Using spatial correlation techniques, particle displacement is obtained for each IW. Hence one velocity vector is obtained for each IW. For single frame-double exposure images, autocorrelation is used for obtaining the seeding particle displacement. The velocity vector direction is ambiguous in this method. Double frame-double exposure images were processed using a cross-correlation method, which removes the directional ambiguity that is present in autocorrelation.

The time interval between the laser illuminations must be such that it is short enough to prevent particles with out-of-plane velocity from leaving the light sheet while

long enough to determine the displacement with sufficient resolution. For resolving small scale structures in the fluid flow, the IW has to be small, while it should contain enough particles for a successful correlation. Overlapping the IW during image processing allows for more particles for calculating the local velocity vector. Since only positions at two successive time steps are known, any velocity curvature information between these positions will be lost. Hence in regions of flow changes such as vortices, the time interval should be small enough such that it is able to resolve those structures. The seeding density should not be high enough to cause difficulties in matching up the same particle for displacement calculations. By using virtual techniques like window overlapping to increase particle number in an IW, problems like correlation errors and particle agglomeration can be avoided.

B. PIV Results

For the PIV measurements without an active ionic wind, the effects of the electrodes on the flow were found to be limited to a small region near the test section centerline (the electrode plane). Fluid flow near the walls was unaffected by the

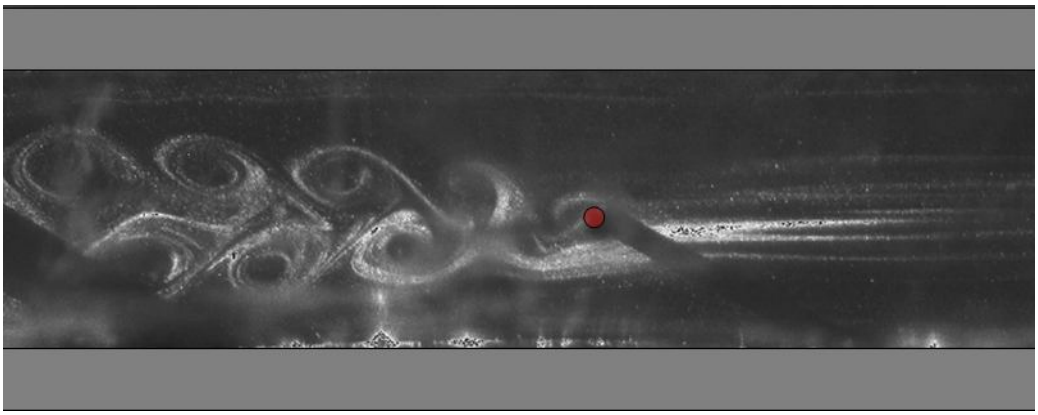

Figure 3-5 Vortex shedding observed in the flow channel in the absence of ionic wind. Red dot indicates the collecting electrode.

presence of electrodes. Vortex shedding was observed through smoke visualization (Fig. 3-5), as anticipated, but notably, it was present only when the ionic wind was not activated. The bulk fluid velocity was determined based on these measurements done upstream of electrodes (without activating ionic wind). More information about the bulk flows are given in Appendix B.

The impact of the ionic wind on 1.2 m/s bulk flow was found to be significant. As shown in Fig. 3-6, the flow was accelerated away from the centerline and impinged on the walls of the flow channel. At a greater corona current (40 μA), the ionic wind velocity became comparable to the bulk flow, and recirculation zones were formed at four locations near the electrodes – two sets of symmetric recirculation zones across the centerline. The recirculation appears typical of those due to an impinging flow, and the first set appears upstream of the collector electrode. This flow recirculation generally caused the flow near the wall to significantly slow down upstream of the electrodes, including some flow reversal, and adversely affected convection. The second set of recirculation zones appears between the two electrodes, and it was near these

recirculation zones that the bulk flow was directed towards the walls and thus resulted in increased cooling. Of note is the position of the recirculation zones relative to the flow channel walls. In an impinging flow in a static environment, two wall jets of equal magnitude are formed resulting in symmetric recirculation zones across the impingement axis. However, that is not the case here. The upstream set of recirculation zones was formed very close to the walls, similar to a wall jet. On the other hand, the second, downstream set was further from the wall, approximately halfway between the walls and the centerline. The presence of the bulk flow requires mass conservation, and therefore the downstream wall jet had a much faster speed than the upstream (reversed) wall jet. This accelerated wall jet pushed the downstream recirculation zones away from the wall. Additionally, the downstream recirculation zones were influenced by the flow entrained into the counter-flow ionic wind near the collecting electrode, which also pulled them away from the wall.

A different phenomenon was observed at the lower current of 20 μA. The flow was again redirected towards the wall, but does not behave like an impinging flow. There were no upstream recirculation zones, and only smaller downstream recirculation zones existed, due primarily to entrainment by the counter-flow ionic wind. In general, the redirection of the flow caused it to accelerate along the wall, enhancing convection. As the flow impinged on the wall, it was redirected towards the flow channel centerline. At the centerline, these redirected flows met slightly downstream of the electrodes and joined, continuing with comparable velocity to that of the bulk velocity upstream of the electrodes. The velocity was slightly reduced (from the bulk velocity value) along the

centerline while it was slightly increased closer to the wall boundaries. This effect downstream of the electrodes appeared to subside with distance from the electrodes, though it was not measured directly.

When the bulk velocity was increased to 1.7 m/s, however, the effect of the ionic wind was much different (Fig. 3-7). The ionic wind was insufficient to effectively divert the flow toward the wall. However, it created a region of very low flow in the area near the collecting electrodes – essentially a flow blockage. Because of the mass conservation, this flow blockage caused the bulk flow to accelerate through the reduced area between the electrodes and walls. Thus, there was a noticeable acceleration of the flow, increasing by as much 0.5 m/s (~30 %). At a greater corona current (40 μA), the "blockage" was more effective, so the wall acceleration was slightly greater, but not significantly so. These two cases were similar to the 20 μA/1.2 m/s flow in Fig. 3-6, but not comparable to the 40 μA/1.2 m/s flow. From all these measurements, there appears to be a critical matching of the ionic wind flow speed and the bulk speed. When the inertia of the bulk speed dominates, wall acceleration is the primary result, but when the inertia of the ionic wind dominates, an impinging flow is generated.

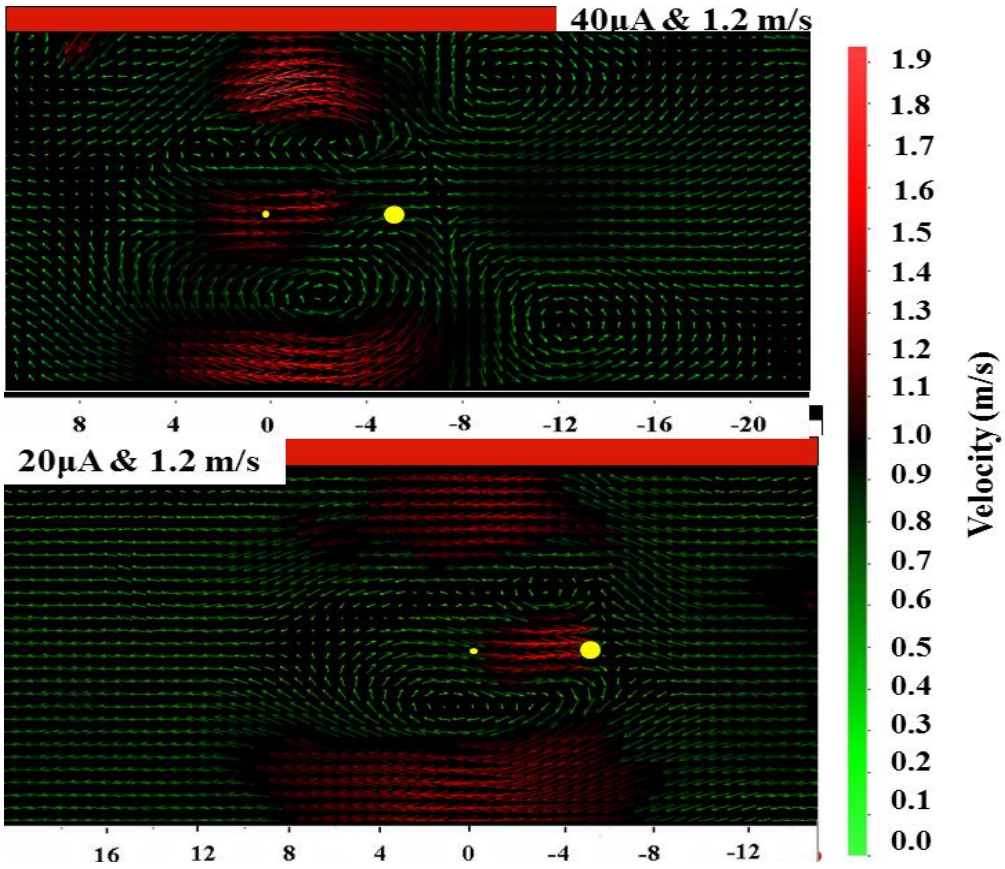

Figure 3-6 PIV images for the case of 1.2 m/s bulk velocity and two corona currents, 20 μA and 40 μA. The larger yellow dot indicates the collecting electrode, and the smaller yellow dot indicates the corona electrode. The bulk flow is from right to left. Distance scales in mm are attached to each plot for reference.

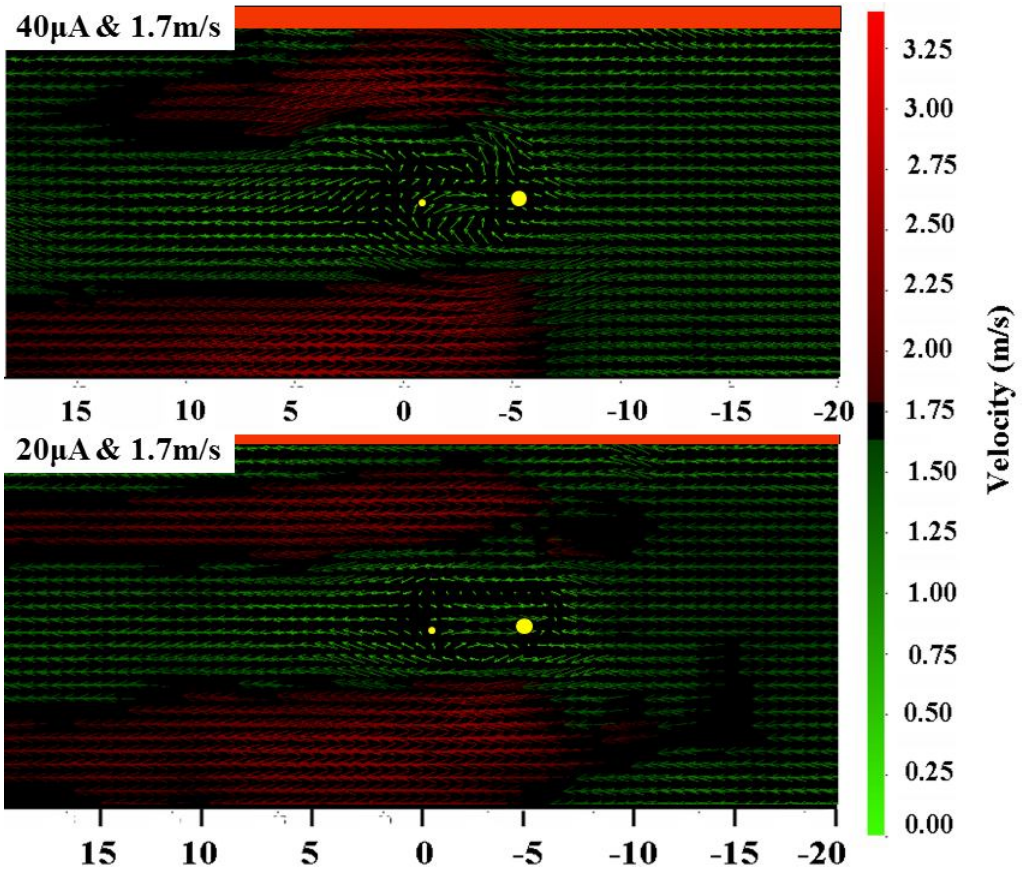

Figure 3-7 PIV images for the case of 1.7 m/s bulk velocity and two corona currents, 20 μA and 40 μA. The larger yellow dot indicates the collecting electrode, and the smaller yellow dot indicates the corona electrode. The bulk flow is from right to left. Distance scales in mm are attached to each plot for reference.

3.4.2 Heat Transfer

For all the cases considered, the ionic wind increased the heat transfer at the location of the thermocouples, causing the steady state wall temperature to drop as shown in Fig. 3-8. Temperature data for all the cases are shown in Tables 3.1 to 3.4. For all cases, the enhancement begins upstream of the electrodes at thermocouple 1 (11 mm upstream of the corona wire) and increases in the flow direction. However, though not directly measured due to the position of the thermocouples, at some downstream

position the effect of the enhancement will diminish. The largest temperature decrease, and thus greatest heat transfer enhancement, was observed for the combination of 40 μA current and 1.2 m/s bulk flow velocity. The other three cases (20 μA/1.2 m/s, 40 μA/1.7 m/s, 20 μA/1.7 m/s) all had a similar smaller effect. These results correlate well with the PIV measurements. Recall that the film heaters extended 31 mm upstream of the electrodes such that the flow experienced heating prior to meeting the counter-flow ionic wind (and locations of the thermocouples). For the three cases of 20 μA/1.2 m/s, 40 μA/1.7 m/s, and 20 μA/1.7 m/s, the counter-flow ionic winds caused the flow to accelerate along the heated wall, increasing the advection and a corresponding increase in heat transfer. A 30 % increase in wall flow speed corresponds to a 30 % increase in Re_L. As the Nusselt number goes with the square root of Reynolds number for external flow ($Nu_L \propto Re_L^{1/2}$), which this flow approximates, only a 14 % increase in heat transfer coefficient was anticipated, accounting for the modest temperature reductions. However, for 40 μA ionic wind and 1.2 m/s bulk flow velocity, the impinging flow actually drew colder flow from the centerline towards the wall, a phenomenologically different enhancement mechanism where the nature of the flow was fundamentally changed. The impingement of colder air resulted in the greatest heat transfer enhancement in this study. From a design perspective, as noted in the PIV results, this suggests that one of the most important factors in maximizing heat transfer enhancement is generating a counter-flow ionic wind that can overcome the inertia of the bulk to generate an impinging flow.

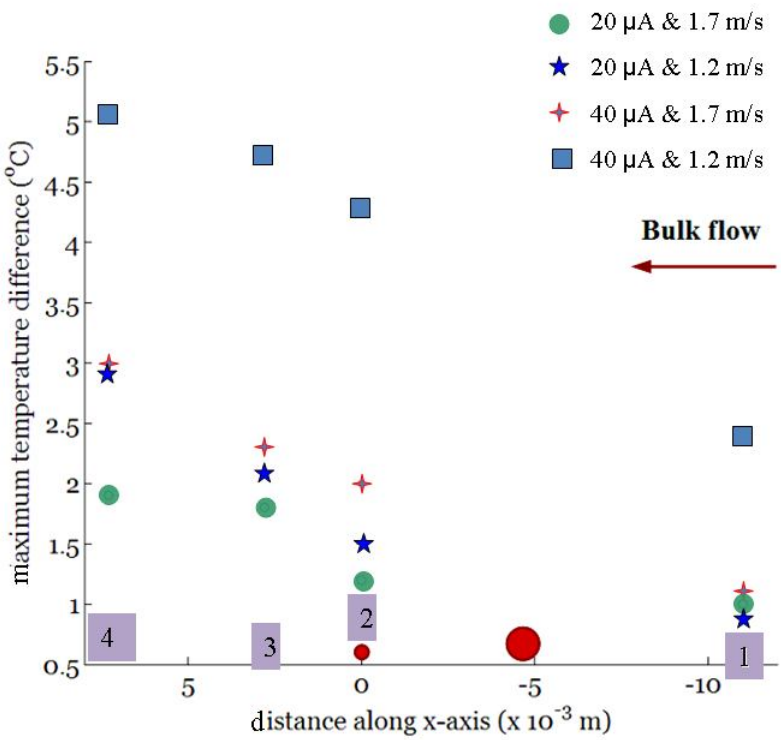

Figure 3-8 Steady state temperature reduction due to counter-flow ionic wind as a function of location corresponding to the four thermocouple locations as noted in the numbered boxes. The larger red dot indicates the collecting electrode, and the smaller red dot indicates the corona electrode, whose center was located at x = 0.

TABLE 3.1: FINAL STEADY STATE TEMPERATURES OF THE HEATED PLATE AT EACH THERMOCOUPLE LOCATION FOR THE CASE OF BULK FLOW ONLY AND BULK FLOW WITH IONIC WIND. BULK FLOW SPEED IS 1.2 m/s. IONIC CURRENT IS 40 μA

Thermocouple location	*1*	*2*	*3*	*4*
Bulk flow (°C)	49.8	53.2	55.3	46.7
Bulk flow with ionic wind (°C)	47.4	48.9	50.6	41.6

TABLE 3.2: FINAL STEADY STATE TEMPERATURES OF THE HEATED PLATE AT EACH THERMOCOUPLE LOCATION FOR THE CASE OF BULK FLOW ONLY AND BULK FLOW WITH IONIC WIND. BULK FLOW SPEED IS 1.7 m/s. IONIC CURRENT IS 40 μA

Thermocouple location	*1*	*2*	*3*	*4*
Bulk flow (°C)	47.2	50.5	52.8	44.8
Bulk flow with ionic wind (°C)	46.1	48.5	50.5	41.8

TABLE 3.3: FINAL STEADY STATE TEMPERATURES OF THE HEATED PLATE AT EACH THERMOCOUPLE LOCATION FOR THE CASE OF BULK FLOW ONLY AND BULK FLOW WITH IONIC WIND. BULK FLOW SPEED IS 1.2 m/s. IONIC CURRENT IS 20 μA

Thermocouple location	*1*	*2*	*3*	*4*
Bulk flow (°C)	47.4	49.5	53.7	46.4
Bulk flow with ionic wind (°C)	46.5	47.4	51.6	43.5

TABLE 3.4: FINAL STEADY STATE TEMPERATURES OF THE HEATED PLATE AT EACH THERMOCOUPLE LOCATION FOR THE CASE OF BULK FLOW ONLY AND BULK FLOW WITH IONIC WIND. BULK FLOW SPEED IS 1.7 m/s. IONIC CURRENT IS 20 μA

Thermocouple location	*1*	*2*	*3*	*4*
Bulk flow (°C)	47.2	50.5	52.8	44.8
Bulk flow with ionic wind (°C)	46.1	48.5	50.5	41.8

The convective coefficient and its enhancement through ionic wind can be calculated by applying an energy balance to the heated plate. It was assumed that the heated plate was radiating to all surfaces (transparent plastic) at the same room

temperature (296 K). The surfaces to which the heated plate was radiating were considered as black bodies. The energy balance for the heated plate is then given by

$$q'' = h_{total}(T_h - T_{bf}) + \sigma\varepsilon_e(T_h^4 - T_{sur}^4) \ , \tag{3.1}$$

where q'' is the heat flux input, h_{total} is the convection coefficient, ε_e is the emissivity of the heated plate (0.96), T_h is the temperature of the heated plate, σ is Stefan-Boltzmann constant (5.67 X 10^{-8} w/m^{2}K^4), T_{bf} is the temperature of the bulk flow, and T_{sur} is the surface temperature to which heated plate is radiating. The power input, P_{in} given to the two heaters was found out by using

$$P_{in} = \frac{V^2}{R}, \tag{3.2}$$

The voltage V of the power source for the heater and the total resistance of the heaters R were measured with the help of a digital multimeter. The two heaters were connected in parallel to the power source. After finding the total resistance using $\frac{1}{R} = \frac{1}{R_1} + \frac{1}{R_2}$, where R_1 and R_2 are the individual resistance of the two heaters, P_{in} was calculated using Eq. 3.2. This power to the heater was assumed to be given fully to the Teflon plate. The conduction from the sides of the heater and the Teflon sheet can be neglected as the conductivity of the surrounding plastic sheet is very low. Thus the obtained value of heat input was 2.3 W. This value was divided by the area of the heated plate (77 mm × 51 mm) to obtain q''. Here it was assumed that the input heat flux to the heated plate (from the heaters) is spatially uniform. This was not strictly true as temperature variations were found along the length of the heater during initial testing.

The convection coefficient in Eq. 3.1, h_{total}, accounts for all modes of convection (forced and free), but it was necessary to determine the relative contribution of free convection. The correlation by Churchill and Ozoe [39] was used for calculating the free convection heat transfer coefficient, h_{free}. The expression is valid for an enclosure with heating from the bottom wall. The Nusselt number for free convection, Nu_{free} is given by

$$Nu_{free} = \left(\left[1 + 1.446 \left(1 - \frac{Ra_c}{Ra_L} \right) \right]^{15} + \left[0.109 Ra_L^{0.313} \right]^{15} \right)^{\frac{1}{15}}, \tag{3.3}$$

where Ra_L is the Rayleigh number based on characteristic length, L, and Ra_c is the critical Rayleigh number for the onset of motion in the enclosure. Ra_c is given by the following empirical correlation[39],

$$Ra_c = 1708 \left(1 + \frac{0.425}{H_1^{1.5}} \right) \left(1 + \frac{3}{H_2^2} \right)^{\frac{1}{4}}, \tag{3.4}$$

where $H_1 = \frac{l}{h}$, $H_2 = \frac{w}{h}$, l is length of the heated plate (77 mm), w is the width of the heated plate (51 mm), and h is the distance between the bottom and the top walls (19 mm). Ra_L value was obtained as 16391.75 and was given by the relation,

$$Ra_L = \frac{g \beta_{te} (T_h - T_{bf}) L^3}{\nu \alpha_{td}}, \tag{3.5}$$

where β_{te} is the thermal coefficient expansion of the fluid, L is given by the ratio of surface area to perimeter [36], ν is the kinematic viscosity of the fluid, and α_{td} is the thermal diffusivity of the fluid. Nu_{free} value was obtained as 2.38 and h_{free} was estimated using the following relation,

$$Nu_{free} = \frac{h_{free} L}{k_f} \quad , \tag{3.6}$$

where k_f is the conductivity of the surrounding fluid. The plate temperature for the calculations for h_{free} was taken as constant at 323 K. All fluid properties required for h_{free} calculations were estimated at film temperature, $T_{f,}$ given by

$$T_f = \frac{T_h + T_{bf}}{2} \quad , \tag{3.7}$$

where T_h was taken as 323 K and T_{bf} as 296 K. h_{free} value of 2.04 was obtained and was comparatively smaller than the forced convection coefficient and hence was not considered further in the calculations. Hence h_{total} represents only the forced convection coefficient from here onwards.

For the case of no ionic wind,

$$h_{total} = h_{bulk} \, , \tag{3.8}$$

where h_{bulk} is the convection heat transfer coefficient in the presence of bulk flow alone. When the ionic wind is switched on, the heat transfer coefficient is enhanced by the ionic wind. As an approximation, the influence of ionic wind on heat transfer enhancement can be estimated using the correlation for transverse flows on flat plates [38],

$$h_{total}^{7/2} = h_{bulk}^{7/2} + h_{ionic}^{7/2} \, , \tag{3.9}$$

where h_{ionic} is the heat transfer coefficient due to ionic wind alone. Assuming h_{bulk} remains of the same value when an ionic wind is switched on, h_{ionic} can be estimated. h_{bulk} was calculated with the temperature data for the case of bulk flow alone using Eq.

(3.1) and Eq. (3.3). h_{total} was calculated with the temperature data for the case of bulk flow in the presence of ionic wind using Eq. (3.1). This value of h_{total} has components of h_{bulk} and h_{ionic} and h_{ionic} was then estimated using Eq. (3.9) as other two values are known. The accuracy of Eq. (3.9) should be more for the impingement case of ionic wind interaction compared to the flow blockage case. This is so since the ionic flow near the wall surface resembles a transverse flow most closely for the impingement case.

Heat transfer coefficients for each combination of bulk velocities (1.2 m/s and 1.7 m/s) and ionic velocities (40 μA and 20 μA) were plotted (Fig 3-9 to 3-12). In these figures, the larger red dot indicates the collecting electrode, and the smaller red dot indicates the corona electrode, whose center was located at x = 0. Thermocouple locations are indicated by numbers, 1 to 4 [refer Fig. 3-3] in the figures. From these plots, it can be seen that the heat transfer enhancement from ionic wind component (through transverse flow) increases as the ionic current increases. From PIV results (Fig. 3-6 to 3-7), it can be seen that ionic wind velocity is more than or comparable to the bulk flow velocity for the case of 40 μA current. When bulk flow is 1.2 m/s, h_{ionic} exceeds h_{bulk} at all locations (thermocouple) except at the upstream section. For Fig. 3-10, the bulk velocity has been increased to 1.7 m/s. At the downstream location, h_{ionic} is still comparable to h_{bulk} in this case. At other thermocouple locations, it can be seen that effect of ionic wind is less significant and h_{bulk} is greater than h_{ionic} at these locations, with the greatest difference found at the upstream location. For the lower ionic wind cases (Fig. 3-11 to 3-12), h_{ionic} is generally lower than h_{bulk} suggesting reduced ionic wind influence which correlates well with the PIV results (Fig. 3-7). However, as the bulk

velocity was also decreased, h_{ionic} became comparable to h_{bulk} at the downstream location (thermocouple 4). The heating given to the plate from the heater was assumed to be uniform spatially for these calculations. The lower heat transfer coefficient (Fig 3-9 to 3-12) at location of thermocouple 3 as compared to that at thermocouple 1 and 2 is probably due to the non-uniformity in heat flux. This will be clearer on calculations of percentage enhancement of heat transfer coefficient at the same thermocouple locations.

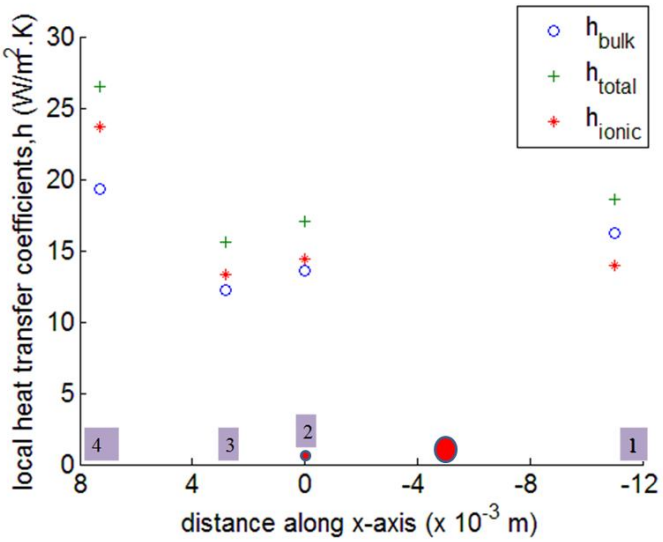

Figure 3-9 Heat transfer coefficients at each of the thermocouple locations for the case of 40 µA and 1.2 m/s.

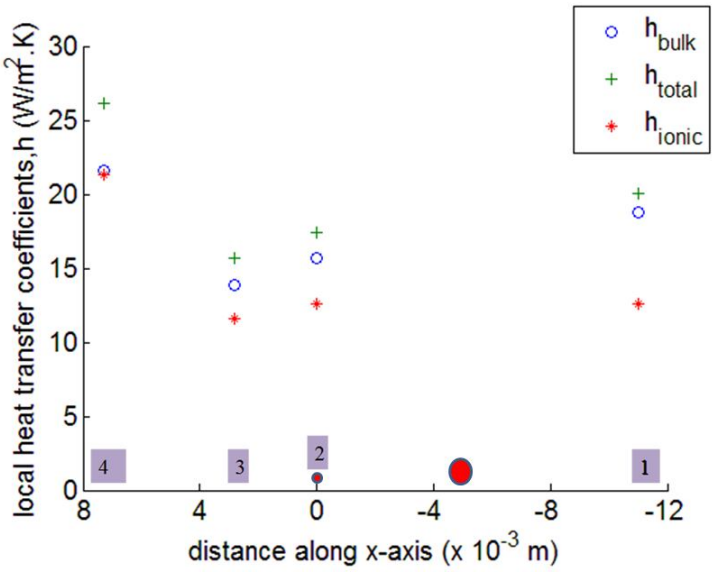

Figure 3-10 Heat transfer coefficients at each of the thermocouple locations for the case of 40 µA and 1.7 m/s.

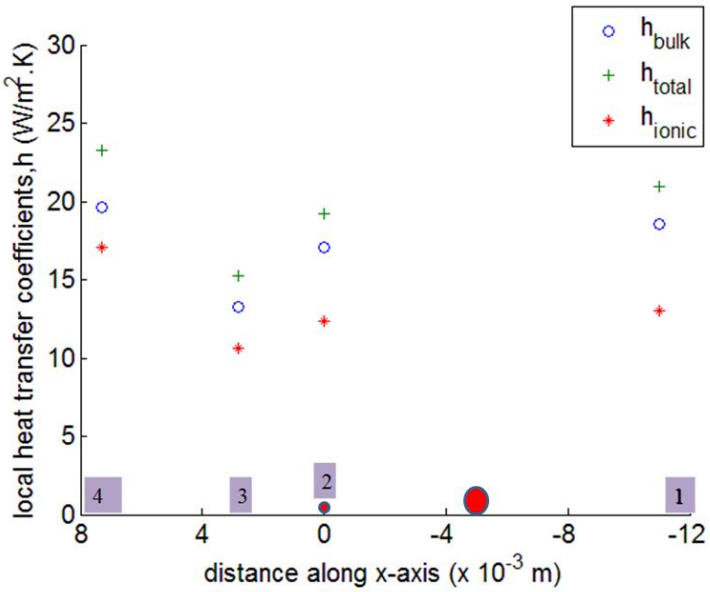

Figure 3-11 Heat transfer coefficients at each of the thermocouple locations for the case of 20 µA and 1.7 m/s.

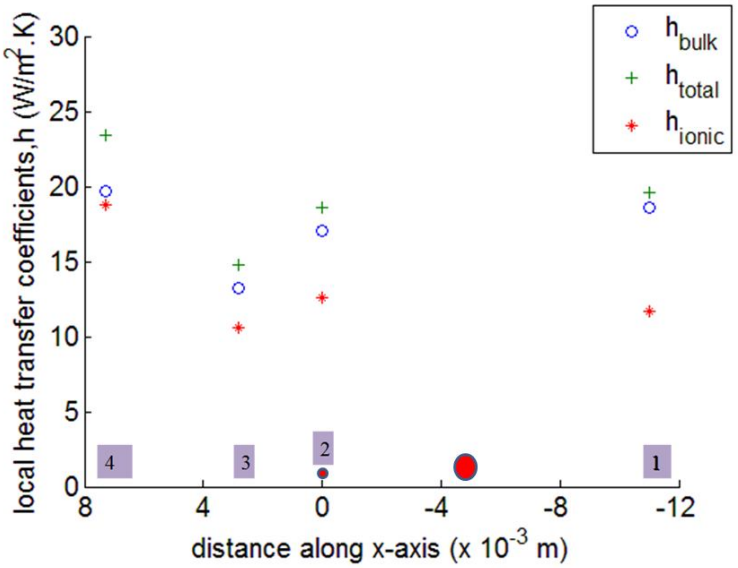

Figure 3-12 Heat transfer coefficients at each of the thermocouple locations for the case of 20 µA and 1.2 m/s.

N_{EHD} was found to be the highest for the 40 µA and 1.2 m/s combination, equaling 3.92. It was lowest for 20 µA and 1.7 m/s bulk velocity combination, having a value of 0.765. For a bulk velocity of 1.2 m/s, this value of ionic current showed a N_{EHD} value of 1.96. For 40 µA and 1.7 m/s, N_{EHD} value was 1.53. Larger values of N_{EHD} numbers indicate higher influence of the ionic wind on the bulk flow. For the same ionic current, lower bulk flow velocities result in higher N_{EHD} numbers. Also for the same bulk velocity, higher ionic current results in higher N_{EHD} numbers. It was observed that generally, higher N_{EHD} numbers resulted in higher heat transfer enhancement.

The effect of counter-flow ionic winds for the two different bulk velocities are shown in Fig. 3-13. The heat transfer coefficient enhancement, κ, is plotted in percentage for each thermocouple location where

$$\kappa = \frac{h_{total} - h_{bulk}}{h_{bulk}}, \tag{3.10}$$

For both bulk velocities, an increase of ionic wind velocity resulted in an increase in κ.

This suggests that the ratio of ionic velocity/bulk velocity is important in determining the amount of heat transfer. Visualization images show that this is due to the different flow structures that result from this ratio. For the case of 40 μA and 1.2 m/s, the enhancement percentage has reached a value of around 36 % at the downstream location, the highest enhancement observed (Fig. 3-13). For the case of 1.7 m/s, the enhancement percentage has reached a value of around 20%. For the case of 40 μA and 1.7 m/s and 20 μA and 1.2 m/s, the enhancement percentages show a similar trend over all the locations suggesting ionic velocity to bulk velocity ratio is an important parameter.

In Fig. 3-13, the local heat transfer coefficient enhancement gradually increases from upstream of the electrodes towards downstream. The spatial non-uniformity of the heater input (to the heater plate) is not a factor in this plot as coefficient change is plotted for each location. As a result this plot gives an accurate picture of the effect of ionic wind along the heated plate. The κ values are found to increase downstream of electrode locations.

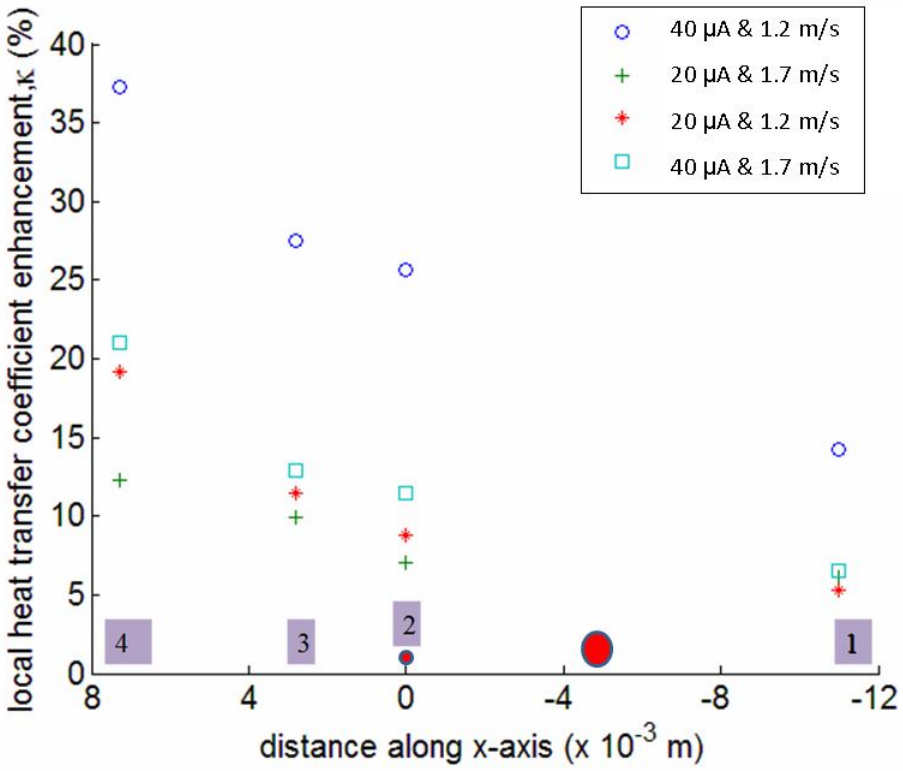

Figure 3-13 Heat transfer coefficient enhancement shown for all cases. Thermocouple locations are indicated in the numbered boxes [refer Fig. 3-3]. The larger red dot indicates the collecting electrode, and the smaller red dot indicates the corona electrode, whose center was located at x = 0.

CHAPTER 4:

PARTICLE TRACKING

4.1 Overview

PIV requires the introduction of seeding particles into the fluid flow for measurement purposes, and the measurement assumes these seeding particles follow the fluid motion. However, as the particles pass through a corona discharge, they could become charged, and Coulombic forces due to the electric field may cause the seeding particles to deviate from the bulk fluid flow, skewing the accuracy of PIV measurements. Attempts have been made by some researchers to optimize seeding particles for use in PIV in non-thermal plasma discharges [40]. Another study reported the usage of PIV to study flow velocities in an electrostatic precipitator (ESP) model [41], reporting that the seeding particles were affected by the charges and the electric field. In order to have confidence in the fidelity of these PIV results, a model studying the influence of charging and the electric field on seeding particles was constructed. To simplify modeling, a co-flow scenario was assumed, but the results suggest that the counter-flow configuration in the experiments does not behave appreciably differently.

In this chapter, a background on particle charging is given next. The particle tracking model is elaborated with a focus on electric field simulation and particle motion, and thereafter, results follow.

4.2 Background

Particle charging can occur by many mechanisms such as attachment of ions and static electrification. The most common mechanism of charging is ion attachment [42] and it has two main modes – diffusion charging and field charging.

Diffusion charging occurs due to Brownian motion of ions and particles. Unipolar ions undergo random collisions with particles and the particle becomes charged by these colliding ions. Diffusion charging becomes prominent for particles < 0.1 μm in diameter, even if an electric field is present. For seeding particles generated from smoke, most of the particles will be almost an order of magnitude greater than this value [43] such that diffusion charging is negligible. Field charging occurs due to electric field in the medium. If permittivity of the particle is higher than that of the medium surrounding it, the field lines will converge towards it, and ions will travel along these field lines toward the particle. Fig. 4-1 shows the field lines near a particle of relative permittivity, $\varepsilon_r > 1$. For $\varepsilon_r = 1$, there will not be any field line convergence. The distortion of the field depends upon the relative permittivity and number of charges on the particle. Once the particle starts getting charged, the charges on the particle tend to repel the incoming ions. After a certain amount of charging, the field due to the charges on the particle will not allow any incoming field lines to converge on it as shown in Fig.

4-1. Field directed ion-particle collision will not occur after this point. Thus, as the particle gets charged, the rate of field charging decreases and comes to zero.

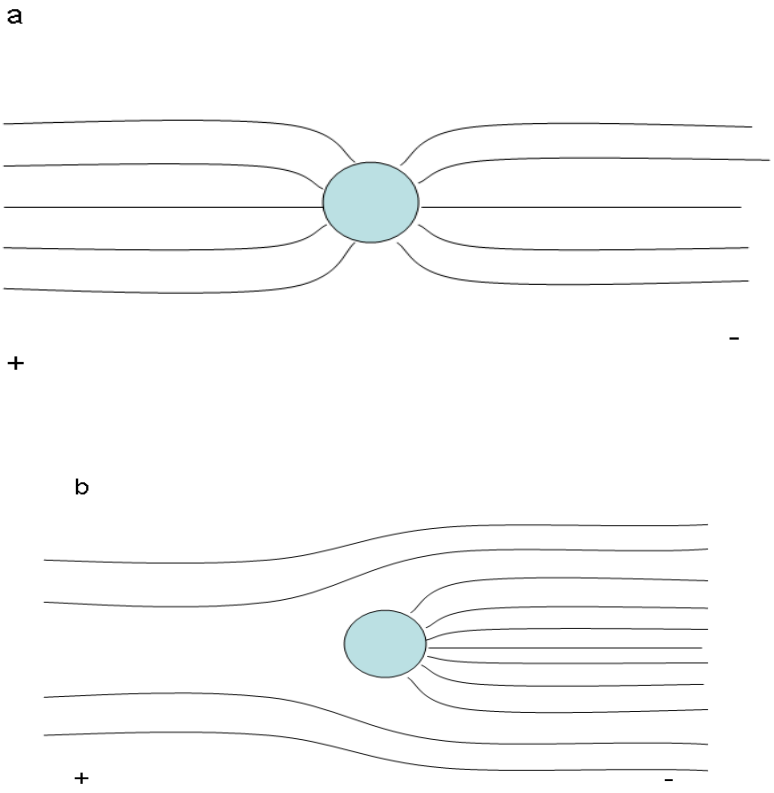

Figure 4-1 Electric field lines near the particle (a)When the particle has zero charges (b) After reaching saturation charge.

A good review of various particle charging models including field charging theory, diffusion charging theory and combined field-diffusion theory have been enumerated in the paper by Long et al. [44]. Nine particle charging models were evaluated and results were compared to experimental data available elsewhere. For combined field-diffusion charging models, the model by Lawless et al. [45] was recommended for numerical models. However this is considering all the factors of theoretical completeness, accuracy and computational time. Even though some

charging models were found more accurate, no charging model was able to predict all the experimental results accurately. In his work, Lawless et al. [45] considered "field assisted" diffusion charging in addition to standard diffusion charging and field charging. When the particle is charged to saturation value as predicted by the Pauthenier theory, all field directed ion flow to the particle ceases. However, near the front edge of the particle and upstream of it, the ion density is still the same as before saturation of charge. The ion density gradient present near the edge can still result in charges reaching the particle surface through diffusion (after saturation value see fig). Upstream surface of the particle is assumed to receive most of the field assisted charging.

Diffusive charging is modeled by researchers in two ways. Works by White et al. [46], Smith et al. [47] and Liu et al. [48] considered that kinetic collisions of ions with the particle was the cause of diffusion charging. Liu et al. [49] and Fjeld et al. [50] considered diffusion charging as driven by ion density gradient near the particle surface. This approach is applicable if particle diameter is much larger than ion radius. Lawless et al. [45] considered the latter type for his modeling. This two approaches are on the basis that collision between ions and particles occur in three regimes depending on the magnitude of the Knudsen number, $Kn = \lambda_i/a$, where λ_i is mean free path of ions and a is radius of the particle [51]. For $Kn << 1$, the collisions happen in continuum regime and are diffusion controlled. For $Kn >> 1$, kinetic theory of gases must be used to explain the collisions which are happening in the molecular regime. Equation derived by White [52] is widely used for diffusion charging, which was derived for the continuum regime.

$$n_d = \frac{d_p kT}{2K_E e^2} \ln\left(1 + \frac{\pi K_E d_p \bar{c}_i e^2 N t}{2kT}\right), \tag{4.1}$$

where d_p is particle diameter, k is Boltzmann's constant (1.3806 x 10-23 J/K), $\bar{c}_i$ is mean thermal speed of the ions, t is time (s), e is elementary charge (1.6×10^{-19} C), N is ion number density, T is the operating temperature (K), and K_E is an electrostatic constant given by $1/4\pi\varepsilon_0$.

Field charging is the result of directed ion-particle collisions, and it is the primary charging mechanism for particle diameters > 0.4 μm when at least a moderate field is present. Hence in this simulation only field charging was considered. Field charging was modeled using Pauthenier theory [53], which states that given sufficient time for charging, a spherical particle will reach a maximum total charge, p_{max} (C), known as the Pauthenier limit, and it is directly proportional to the electric field,

$$p_{\max} = 4\pi\varepsilon_0 a^2 E \frac{3\varepsilon_p}{\varepsilon_p + 2\varepsilon_0}, \tag{4.2}$$

where ε_p is the dielectric permittivity of the particle (F/m) and a is the radius of the particle (m). The amount of charge p (C) acquired by the spherical particle through field charging is given by

$$p = p_{\max} \frac{t}{t + 4\varepsilon_0 / e\mu_E N}, \tag{4.3}$$

4.3 Model

A. Particle Force Balance

To simulate the motion of a charged particle, an equation of motion based on the Basset-Boussinesq-Oseen (BBO) equation was used [54]. The BBO equation describes the general (linear) equation of motion for a small spherical particle suspended in a fluid.

$$\frac{\pi}{6} d_p^3 \rho_p \frac{dU_p}{dt} = -3\pi\mu d(U_p - U) + \frac{\pi d_p^3}{6}\rho_f \frac{dU}{dt} - \frac{1}{2}\frac{\pi d_p^3}{6}\rho_f \frac{d(U_p - U)}{dt} + \sum_i F_i , \qquad (4.4)$$

where d_p is diameter of the particle (m), ρ_p is mass density of the particle (kg/m^3), U_p is particle velocity (m/s), t is time (s), U is fluid velocity (m/s), ρ_f is fluid density (kg/m^3), and F_i denotes other external forces. The terms on the right hand side (RHS) are forces due to Stokes drag, pressure gradient, added mass, and other external forces respectively. Particle Reynolds number was obtained as 5.4×10^{-3} (<< 1) for a relative velocity of 0.1 m/s, and hence Stokes law (drag force) is valid. The Coulombic force resulting from the presence of charges and electric field appears as an external force in the equation. Dielectrophoretic forces, which arise from permittivity gradients, were not taken into consideration as the permittivity variation was neglected, and for the same reason, the electrostrictive force was also not taken into account. The drag and Coulombic force terms were the only terms considered. The added mass term and the pressure term were either negligible (compared to the drag force and Coulombic force) or does not enter into the problem due to the fluid flow characteristics (uniform and steady flow) assumed. Therefore the equation of motion in *x*-direction becomes

$$\frac{\pi}{6} d_p^3 \rho_p \frac{dU_{p,x}}{dt} = -3\pi\mu d(U_{p,x} - U_x) + E_x ne \ , \tag{4.5}$$

Similarly, in the *y*-direction normal to the flow channel walls, it becomes of the form

$$\frac{\pi}{6} d_p^3 \rho_p \frac{dU_{p,y}}{dt} = -3\pi\mu d U_{p,y} + E_y ne \, , \tag{4.6}$$

where *n* is number of charges on the particle, *E* is electric field (V/m), and subscripts *p*, *x*, and *y* denote particle, *x*-direction and *y*-direction respectively. For these simulations, the bulk fluid was assumed to have a zero velocity in the *y*-direction so that terms having bulk velocity dropped out of the equation of motion in *y*-direction. The gravity term was found to be negligible compared to other terms and was neglected for this simulation.

These two equations were solved for *x* and *y* velocity and subsequently for *x* and *y* positions as a function of time through direct integration. A fourth order Range-Kutta method was implemented in Matlab for integration [See Appendix for particle tracking code]. Initial condition for particle speed was given same as that of bulk velocity which has velocity component in the *x*-direction only. Since the electric field and corona-generated ions are primarily confined to the region between the electrodes, it was assumed that the seeding particle does not get charged until it has reached the location of the electrodes. The initial location of the particle was aligned with the corona wire, and the motion was tracked until the particle had passed the collecting electrode where electric field becomes negligible. The electrode separation was 5 mm, and the bulk fluid

velocity was set at 2 m/s. The seeding particle size was assumed to be 1 μm and the density was assumed to be 1100 kg/m^3 [55].

B. Electric Field

The critical force in the two BBO equations is the Coulombic force due to electric field, and the field was determined using multi-physics modeling and engineering simulation software COMSOL. The governing equations for the electric field (Poisson's) and ion transport (Eqs. 2.2 and 2.4) were solved to produce the ion concentration and potential field. The electric field was found using Eq. 2.3.

For solving the space charge equation (Eq. 2.4), two methods can be used. These methods both focus on how to apply a suitable boundary condition for the ion concentration, as the space charge density on the corona electrode is not known in advance. One method makes use of Kaptsov's assumption [56]. Kaptsov's assumption states that the electric field at the surface of ionization sheath near the corona electrode remains constant once the corona onsets, regardless of the applied potential, and Peek solved the electric field at the surface of a corona electrode [7], E_0, and for a wire-cylinder electrode configuration in air at standard conditions it's value is given by

$$E_0 = E_c \cdot \left(1 + \frac{0.0262}{\sqrt{R_0}}\right), \tag{4.7}$$

where E_c is breakdown electric field strength for air, R_0 is wire radius. Kaptzov's assumption can be used to link E_0 with the electric field at the interface between the ionization and drift regions, E_i using

$$E_0.R_0 = E_i R_i \ , \tag{4.8}$$

where R_i is the radius of the ionization zone. Because the ionization zone is very narrow in a positive corona compared to the drift region, it is usually neglected in simulations [59]. From these assumptions it can be considered that the electric field at the surface of corona electrode will remain at the value at corona onset voltage [57], regardless of the applied potential between the corona and collecting electrodes. The charge density at corona electrode can be varied in such a way as to match the electric field obtained from Eq. (4.7) at the corona electrode boundary. In the other method, the charge density at the corona electrode is varied so as to match the numerical current with that known from the experiment [58].

For a corona discharge, the ionization zone is very small compared to the drift zone and hence is usually neglected in corona simulations [59]. Hence the source term in Eq. (2.5) becomes zero in the simulation domain being considered. Steady state ion transport was considered. Hence Eq. (2.4) and Eq. (2.5) can be modified for use in COMSOL as

$$\vec{\nabla} \cdot \left(\mu_E \vec{E} q - D \vec{\nabla} q \right) = 0 , \tag{4.9}$$

The value of μ_E used was 2×10^{-4} m^2 $V^{-1}s^{-1}$ [60]. Here advection term in Eq. (2.4) has been neglected as explained in section 2.2.1. Eq. (2.2) and Eq. (2.3) were solved in COMSOL to obtain the electric field during corona discharge. At the inlet, outlet, and walls, a homogenous Neumann condition was used for Poisson's equation and Dirichlet conditions were used on the two electrodes. For the ion transport equation, Kaptsov's

assumption and Peek's critical electric field were employed. A Dirichlet boundary condition for the charge density q at the corona electrode region was adjusted such that the electric field at the electrode surface, when solved self-consistently using Poisson's equation, matched the critical field determined from Eq. (4.7), 2.07 x 10^7 V/m. Current density was assumed to be zero at the wall boundaries and at the inlet and outlet (homogeneous Dirichlet), and a homogenous Neumann condition was assumed for the collecting electrode [59]. This is valid as the diffusion term in the current equation is negligible compared to the drift term [61].

The diameter used in modeling the corona electrode and collecting electrode were 50 μm and 1 mm respectively. The tunnel height and length used were 20 mm and 200 mm. A high mesh density was used near the electrodes where field variation is expected to be high as shown in Fig. 4-2. Further increase in mesh density did not cause any appreciable change in the results. Iterations were conducted till the results showed convergence. This was confirmed as the error graph obtained from COMSOL showed error values below 10^{-14} and stayed around that order.

C. Charging and Tracking

Some assumptions were made for this theoretical study of charging of seeding particles.

(1) Particles were assumed to be spherical.

(2) Particles were assumed to be monodisperse.

(3) Interaction between individual particles was neglected.

(4) The ion concentration was assumed to be uniform throughout the drift region.

(5) Variation of electric field due to the presence of seeding particles was neglected. Due to permittivity difference with the surrounding medium, the field lines will converge a little. However due to the low number density of seeding particles, this distortion of the electric field will be negligible.

These assumptions essentially hold true for most cases of aerosol charging [62].

The amount of charge, $p = n \times e$ was determined using Eqs. (4.2) and (4.3). This was used in calculations at each time step t in the integration of Eqs. (4.5) and (4.6) based on the local electric field calculated by Eq. (2.3).

TABLE 4.1: VALUES FOR IMPORTANT PARAMETERS USED IN THE SIMULATION

Electrode details		
1	Corona electrode diameter	50 µm
2	Collecting electrode diameter	1 mm
3	Electrode separation	5 mm
Seeding particle		
4	Density	1100 Kg/m^3 [55]
5	Size	1 µm
Other details		
6	Ion number density	10^{13} per m^3 [64]
7	Tunnel height	20 mm
8	Tunnel length	200 mm
9	ε_0	8.85×10^{-12} F/m
10	ε_p	35.515×10^{-12} F/m
11	Time step size	1.0002×10^{-6} S
12	μ_E	2×10^{-4} m^2 V^{-1}s^{-1} [60]
13	Charge density at corona electrode surface	10^{-5} C/m^3
14	Applied voltage	5000 V
15	Critical electric field	3.23×10^6 V/m
16	Bulk velocity	2 m/s in x -direction

The amount of charge that can accumulate on the seeding particle due to diffusion charging was studied using Eq. (4.1). For 3.5 ms, the number of elementary charges that can accumulate was found to be ~6. Hence diffusion charging will not be influencing the results significantly. Field charging factor, F_{cf} [63] was calculated to see if field charging was prominent, where

$$F_{cf} = \frac{eEa}{kT}, \tag{4.10}$$

where k is Boltzmann constant and a is particle radius. Calculating, it was found that this factor will be greater than 1 and hence field charging dominant, if electric field is around 10^5 V/m or higher.

The electric field obtained from COMSOL was exported to Matlab for particle tracking. Time step used for the simulation was 1.0002 x 10^{-6} s. Maximum saturation field charge value was calculated using Eq. (4.2). ε_0 and ε_p values used were 8.85 x 10^{-12} F/m and 35.315 x 10^{-12} F/m respectively. N value used was 10^{13} #/m^3 was used [64]. The particle position was calculated at each time step. The field value at the particle location was used for calculating the maximum charge attainable by the particle at each time step. Thus charge accumulated was calculated for each time step. This charge value was added to the previous charge value and after rounding off was used in the integrating steps for velocity. All relevant simulation parameters are listed in Table 4.1.

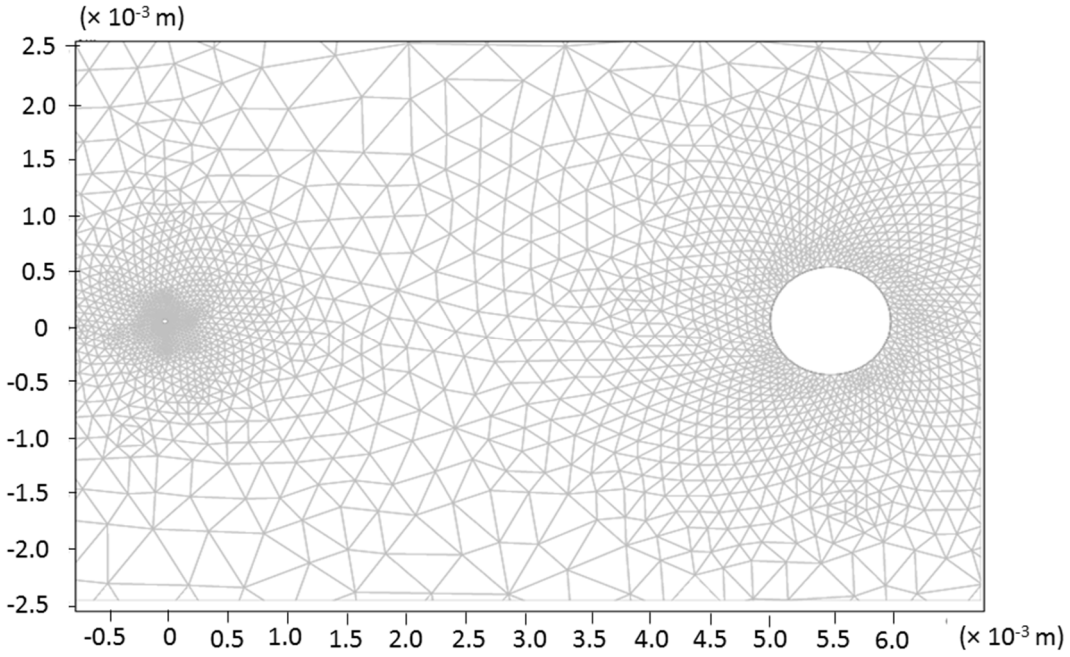

Figure 4-2 Mesh used for solving the electric field. Higher mesh density is used near the electrodes.

4.4 Results

The obtained electric field is shown in close up in Fig. 4-3. It can be observed that the field value near the corona electrode shows the sharpest variation. The field near the collecting electrode also showed variation, though not on the scale of variation near the corona electrode. As expected, electric field is very high near the corona electrode and drops sharply towards the collecting electrode (Fig. 4-4).

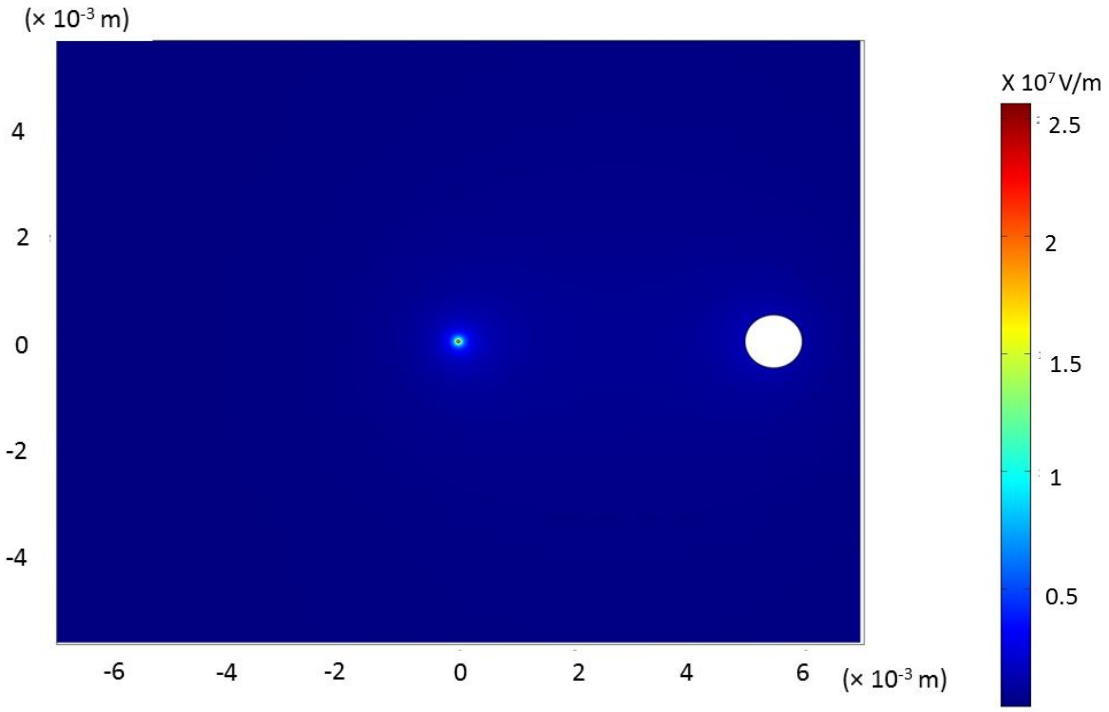

Figure 4-3 Electric field map obtained from COMSOL for the wire-electrode geometry corona.

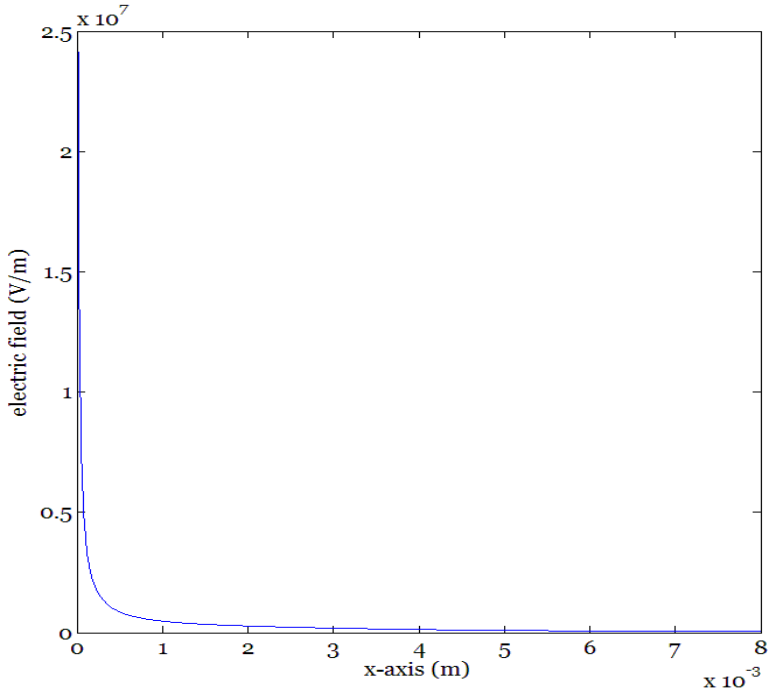

Figure 4-4 Electric field along x-axis.

Charging was found to be prominent only in positions very near the corona electrode where the field was very high, on the order of 10^6 to 10^7 V/m in this study. As this is a corona discharge, the field rapidly decreases towards the collector electrode, where the field was of the order of 10^3 V/m. Hence the charging rate reduced significantly as the particle moved away from the corona electrode. From Fig. 4-5, the maximum number of charges acquired by the seeding particle was ~15 over 3.5 ms, which corresponds to a distance of ~7 mm, covering the electrode separation. This maximum number of charges was for a seeding particle whose initial position was in the vicinity of the electrode plane. For a seeding particle whose position was further away from the electrode plane (that is, between the electrodes and walls), the field charging would become negligible because the electric field was significantly smaller in those regions.

The corresponding deviation of the particle velocity from that of the bulk fluid was found to be minimal in both the *x* and *y* directions (Fig. 4-6). The initial jump in deviation is because the particle starts with the same velocity as that of the fluid. Hence there is no drag force to oppose the Coulombic force in the initial time steps. Also the magnitude of the drag force depends on the relative velocity that exists between the particle and the bulk velocity. This in turn depends on the Coulombic force. If velocity deviation has increased in a time step, the drag force magnitude will be higher in the next step and will bring down the velocity deviation. However, as deviation decreases, drag force also decreases and a jump in velocity deviation occurs in the next time step. Hence a zig-zag pattern in the velocity deviation plot is visible. But this oscillation is a numerical artifact, and it decreases on reduction of the time step used in the integration. The particle trajectory of the seeding particle is plotted in Fig. 4-7. A small deviation of the order of 10^{-4} m in y direction can be observed. Since the initial particle location was in the vicinity of the high field corona region, the deviation is larger than that expected for a counter-flow case. Additionally, the majority of seeding particles do not pass close to the corona electrode where the electric field is highest. For a seeding particle with the worst case of n = 15 charges and a velocity deviation of say, 0.1 m/s at a location where field value is 10^5 V/m as is the case in the majority of the electrode gap, the drag force/Coulombic force ratio is ~75, suggesting minimal impact on the seeding particle tracking the flow. Hence the influence of the corona discharge environment should have negligible influence on the majority of the seeding particles used for these PIV studies.

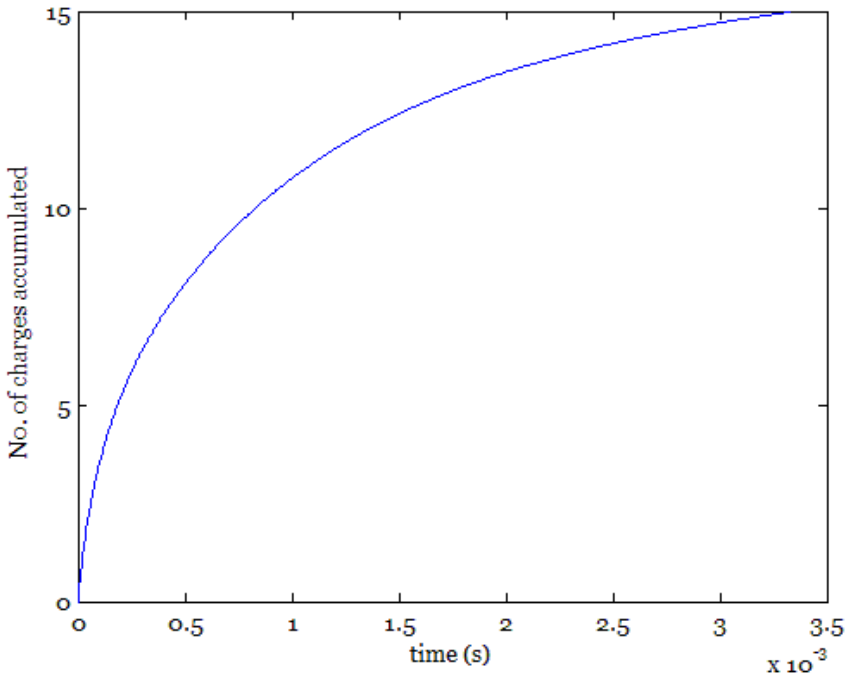

Figure 4-5 Charge accumulation on a seeding particle in a corona discharge environment as a function of time for an initial position immediately adjacent to the corona electrode.

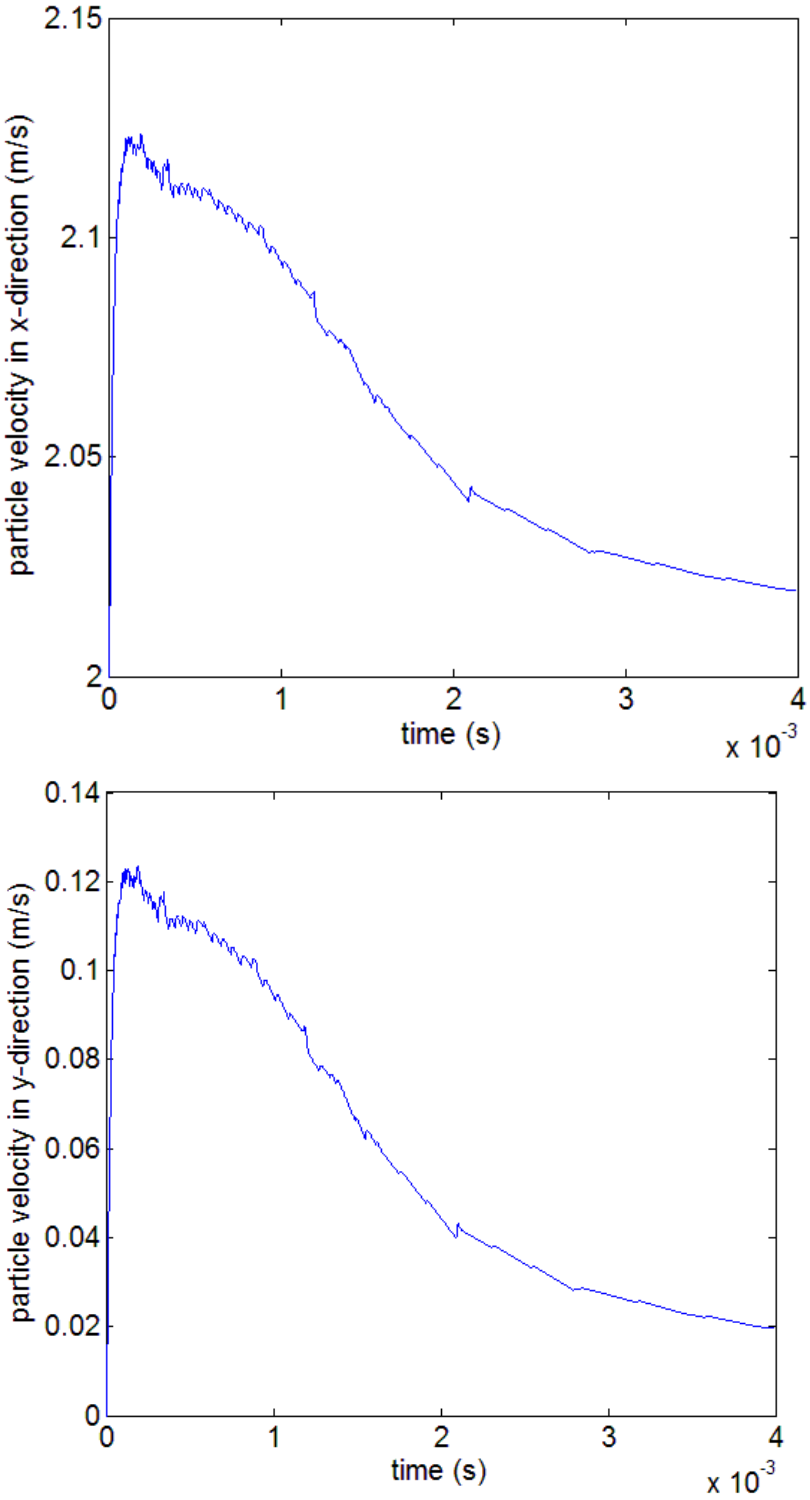

Figure 4-6 Deviation in the x and y velocities of the particle from the corresponding bulk fluid velocities.

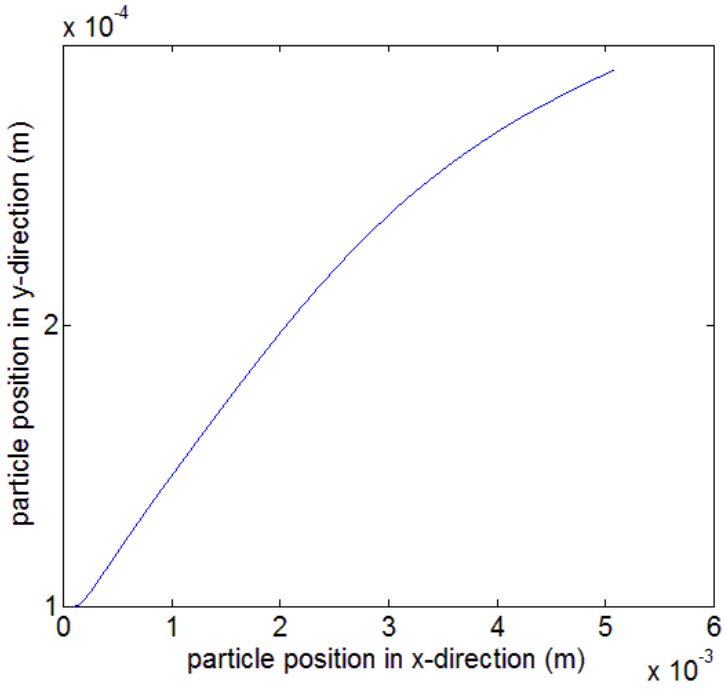

Figure 4-7 Particle trajectory of the seeding particle.

CHAPTER 5:

CONCLUSION

5.1 Overview

This chapter concludes this thesis. A summary of research results are presented, followed by a brief look into the need for future work and recommendations.

5.2 Conclusion

Counter-flow ionic wind was successfully applied for heat transfer enhancement. The counter-flow ionic was found to have potential applications in the cooling of electronic devices, especially those in the consumer portable segment. Particle tracking results and visualization images showed that PIV can be applied with sufficient confidence to corona discharge environments. For majority of the seeding particles, which are away from the electrodes, the effect of charging will be negligible. Ionic wind enhancement becomes less effective as *Re* of the bulk flow increases. An optimum velocity for maximum cooling should exist for each set up of ionic wind enhanced heat transfer. Heat transfer results obtained were explained on the basis of flow structures with the aid of PIV images. As ionic velocity becomes greater than bulk velocity, the flow structure changes from that resembling a flow blockage to one of impingement,

increasing the cooling effectiveness. Ratio of ionic wind to bulk velocity was therefore found to result in different flow structures.

5.3 Future Work

Implementation of counter-flow ionic wind cooling in practical applications would need a better understanding of the maximum cooling potential of this method. The sufficient cooling performance presented in this work warrants a more thorough understanding of the heat transfer enhancement through ionic wind. Higher cooling performance may be obtained by optimizing factors like separation of electrodes and distance of walls from the electrodes. The distance can be adjusted so that the impingement effect of ionic wind is enhanced. The wall geometry may be modified so as to allow a smooth transition of the resultant flow towards upstream. The recirculation zones formed upstream of the electrodes may be reduced in its intensity through this modification.

Particle tracking model may be made more thorough and accurate to enable corrections of velocity vectors obtained from PIV, especially during cases of longer seeding particle resident time (between electrodes) and higher electric fields. In the charging model used, only field charging was considered. Charging due to diffusion was found to be insignificant. However, field-assisted diffusion charging may be present and the combination of diffusion charging and field assisted diffusion charging may happen to affect the results. This may be more so if the electrode separation is higher, since a higher field would be required for the same amount of corona current. Coupled with the

fact that seeding particle spends more time between the electrodes, charging through all modes require a more careful look. The Navier-Stokes equations with the EHD force term may also be solved to find the actual fluid velocity between the electrodes, rather than using a fixed bulk velocity. This will enhance the accuracy in relative velocities used in the drag force calculations in the tracking simulation.

BIBLIOGRAPHY

[1] R. Tummala, *Fundamentals of Microsystems Packaging*, 1st edition, Mc-Graw Hill, pp. 213-262, 2001.

[2] S. Sathe and B. Sammakia, "A review of recent developments in some practical aspects of air-cooled electronic packages," *Journal of Heat Transfer-Transactions of the ASME*, vol. 120, no. 4, pp. 830–839, 1998.

[3] Y. A. Cengel, *Heat Transfer: A Practical Approach*, 2nd edition, Mc-Graw Hill, pp. 785-842, 2002.

[4] J. Moon, D. Hwang and S. T. Geum, "An EHD gas pump utilizing a ring/needle electrode," *IEEE Transactions on Dielectrics and Electrical Insulation*, vol. 16, no. 2, pp. 352-358, 2009.

[5] A. Fridman and L. Kennedy, *Plasma Physics and Engineering*, 1st edition, CRC press, pp. 8-14, 2004.

[6] J. S. Chang, F. Pontiga, A. Castellanas and P. Atten, "Hysteresis effect of corona discharge in a narrow coaxial wire-pipe discharge tube with gas flow," *IEEE Transactions on Industry Applications*, vol. 32, no. 6, pp. 1250-1256, 1996.

[7] F.W. Peek, *Dielectric Phenomena in High Voltage Engineering*, McGraw-Hill, 1929.

[8] B. Owsenek and J. Seyed-Yagoobi, "Theoretical and experimental study of electrohydrodynamic heat transfer enhancement though wire-plate corona discharge", *Journal of Heat Transfer*, vol. 119, pp. 604–610, 1997.

[9] U. D. Landau and E. M. Lifshitz, *Electrodynamics of Continuous Media*, 1st edition, Pergamon, New York, 1963.

[10] M. M. Ohadi, J. Darabi and B. Roget, "Electrode design, fabrication, and materials science for EHD-enhanced heat and mass transport," *Annual Review of Heat Transfer*, vol. XI, edited by C.L. Tien, Begell House, New York, pp. 563-632, 2001.

[11] E. Moreau, L. Leger and G. Touchard, "Effect of a DC surface-corona discharge on a flat plate boundary layer for air flow velocity up to 25m/s," *Journal of Electrostatics*, vol. 64, no. 3-4, pp. 215-225, 2006.

[12] D. M. Bushnell, “Turbulent drag reduction for external flows,” presented at AIAA 21st Aerospaces sciences meeting, Reno, NV, Jan. 1983, Paper AIAA-83-0227.

[13] M. R. Malik, L. M. Weinstein and M. Y. Hussaini, “Ion wind drag reduction,” presented at AIAA 21st Aerospace sciences meeting, Reno, NV, Jan. 1983, Paper AIAA-83-0231.

[14] S. El-Khabiry and G. M. Colver, "Drag reduction by DC corona discharge along an electrically conductive flat plate for small Reynolds number flow", *Physics of Fluids*, vol. 9, no. 3, pp. 587-599, 1997.

[15] L. Leger, E. Moreau and G. Touchard, “Control of low velocity airflow along a flat plate with a DC electrical discharge”, *IEEE Transactions on Industrial Applications*, vol. 38, pp. 1478–1485, 2002.

[16] G. Artana, J. D’Adamo, L. Léger, E. Moreau and G. Touchard, “Flow control with electrohydrodynamic actuators,” *AIAA Journal*, vol. 40, pp. 1773–1779, 2002.

[17] E. Moreau, “Air control by non-thermal plasma actuators,” *Journal of Physics D: Applied Physics*, vol. 40, no. 3, pp. 605-636, 2007.

[18] G. M. Colver and Y. Nakai, “Flame stabilization by an electrical discharge and flame visualization of the influence of a semi-insulating wall on the ionic wind,” in Proceedings of 13th IEEE-IAS annual Meeting, Toronto, Ontario, Canada, pp. 95-104, 1978.

[19] E. Sher, G. Pinhasi, A. Pokryvailo and R. Bar-On, “Extinction of pool flames by means of a DC electric field,” *Combustion and Flame*, vol. 94, no. 3, pp. 244-252, 1993.

[20] M. Robinson, “Movement of air in the electric wind of the corona discharge”, *Transactions of the American Institute of Electrical Engineers*, vol. 80, no. 54, pp. 143-149, May 1961.

[21] H. Bondar and F. Bastien, “Effect of neutral fluid velocity on direct conversion from electrical to fluid kinetic energy in an electro-fluid-dynamics device,” *Journal of Physics D: Applied Physics*, vol. 19, pp. 1657-1663, 1986.

[22] A. P. Chattock, “On the velocity and mass of ions in the electric wind in air”, *Philosophy Magazine*, vol. 48, 1899.

[23] S.M. Marco and H.R. Velkoff, “Effect of electrostatic fields on free convection heat transfer,” *ASME* Paper No. 63-HT-9, 1963.

[24] M. E. Franke, ”Effect of vortices induced by corona discharge on free-convection heat transfer from a vertical plate,” *Journal of Heat Transfer*, pp. 427-432, Aug. 1969.

[25] M. S. Pour and E. Esmaeilzadeh, "Experimental investigation of convective heat transfer enhancement from 3d shape heat sources by EHD actuator in duct flow", Accepted in *Experimental Thermal and Fluid Science*, 2011.

[26] A. Yehia, A. Mizuno and K. Takashima, "Corona characteristics as influenced by magnitude and direction of the air flow rate in wire-duct reactor", in: Conference Record—IAS Annual Meeting (IEEE Industry Applications Society) 2, 2000, pp. 714–718.

[27] H. Kalman and E. Sher, "Enhancement of heat transfer by means of a corona wind created by a wire electrode and confined wings assembly," *Applied Thermal Engineering*, vol. 21, no. 3, pp. 265-282, 2001.

[28] S. R. Mahmoudi, K. Adamiak, P. Castle and M. Ashjaee, "The effect of corona discharge on free convection heat transfer from a horizontal cylinder", *Experimental Thermal and Fluid Science*, vol. 34, no. 5, pp. 528–537, 2010.

[29] M. Molki and K .L. Bhamidipati, "Enhancement of convective heat transfer in the developing region of circular tubes using corona wind," *International Journal of Heat and Mass Transfer*, vol. 47, pp. 4301-4314, 2004.

[30] A. Yabe, Y. Mori and K. Hijikata,"EHD study of the corona wind between wire and plate electrodes", *AIAA Journal*, vol. 16, no. 4, pp.340-345, 1978.

[31] D. B. Go, R. A. Maturana, T. S. Fisher and S. V. Garimella, "Enhancement of external forced convection by ionic wind," *International Journal of Heat and Mass Transfer*, vol. 51, pp. 6047-6053, 2008.

[32] D. B. Go, S. V. Garimella, T. S. Fisher and R. K. Mongia, "Ionic winds for locally enhanced cooling," *Journal of Applied Physics*, vol. 102, no. 5, article no. 053302, 2007.

[33] P. H. G. Allen and T. G. Karayiannis, "Electrohydrodynamic enhancement of heat transfer and fluid flow," *Heat Recovery Systems & CHP*, vol. 15, no. 5, pp. 389-423, 1995.

[34] S. Laohalertdecha, P. Naphon and S. Wongwises, "A review of electrohydrodynamic enhancement of heat transfer," *Renewable & Sustainable Energy Reviews*, vol. 11, no. 5, pp. 858-876, 2007.

[35] NASA, Data on the emissivity of a variety of black paints, Available: http://masterweb.jpl.nasa.gov/reference/paints.htm

[36] F. P. Incropera and D.P. DeWitt, *Fundamentals of Heat and Mass Transfer*, Wiley, 6th edition, pp. 559-597, 2007.

[37] H. R. Velkoff and R. Godfrey, "Low-velocity heat transfer to a flat plate in the presence of a corona discharge in air," *Journal of Heat Transfer*, vol. 101, pp. 157-163, 1979.

[38] H. R. Velkoff, "Electrofluidmechanics: investigation of the effects of electrostatic fields on heat transfer and boundary layers," Aeronautical systems division, Air force systems command Wright-Patterson AFB, OH, ASD-TDR-62-650, 1962.

[39] E.U. Schlunder, *Heat Exchanger Design Handbook*, 1st edition, Taylor and Francis, 1983.

[40] J. S. Chang, D. Brocilo, K. Urashima, J. Mizeraczyk, J. Dekowski, J. Podlinski, M. Dors, M. Kocik, T. Ohkubo, S. Kanazawa and Y. Nomoto, "Optimization of seed-particle size and density used in Particle Image Velocimetry under corona discharges and non-thermal plasmas," presented at 7th Int. Congress on Optical Particle Characterization, Kyoto, Japan, pp. 32-37, 2004.

[41] J. Mizeraczyk, J. Dekowski, J. Podliński, M. Kocik, T. Ohkubo and S. Kanazawa, "Laser Flow Visualization and Velocity Fields by Particle Image Velocimetry in Electrostatic Precipitator Model," *Journal of Visualization*, vol. 6, no. 2, pp. 125-133, 2003.

[42] S. K. Friedlander, *Smoke*, *Dust and Haze: Fundamentals of Aerosol Dynamics*, 2nd edition, USA: Oxford University Press, pp. 40-50, 2000.

[43] S. W. See, R. Balasubramanian and U.M. Joshi, "Physical characteristics of nanoparticles emitted from incense smoke," *Science and Technology of Advanced Materials*, vol. 8, pp. 25-32, 2007.

[44] Z. Long and Q. Yao, "Evaluation of various particle charging models for simulating particle dynamics in electrostatic precipitators", *Journal of Aerosol Science*, vol. 41, no. 7, pp. 702-718, 2010.

[45] P. H. Lawless, "Particle charging bounds, symmetry relations, and an analytic charging rate model for the continuum regime," *Journal of Aerosol Science*, vol. 27, no. 2, pp. 191-215, 1996.

[46] H.J. White, "Particle charging in electrostatic precipitation," *Transactions of the American Institute of Electrical Engineers*, vol. 70, pp. 1186–1191, 1951.

[47] W.B. Smith and J.R. McDonald, "Development of a theory for the charging of particles by unipolar ions," *Journal of Aerosol Science*, vol. 7, pp. 151–166, 1976.

[48] B.Y.H. Liu and H.C. Yeh, "On the theory of charging of aerosol particles in an electric field," *Journal of Applied Physics*, vol. 39, pp. 1396–1402, 1968.

[49] B.Y.H. Liu and A. Kapadia, "Combined field and diffusion charging of aerosol particles in the continuum regime," *Journal of Aerosol Science*, vol. 9, pp. 227–242, 1978.

[50] R.A. Fjeld and A.R. McFarland, **"**Evaluation of Select Approximations for Calculating Particle Charging Rates in the Continuum Regime**,"** *Aerosol Science and Technology*, vol. 10, pp. 535–549, 1989.

[51] P. Intra and N. Tippayawong, "An Overview of Unipolar Charger Developments for Nanoparticle Charging," *Aerosol and Air Quality Research*, vol. 11, no. 2, pp. 187-209, 2011.

[52] White, H.J., *Industrial Electrostatic Precipitation*, Addison-Wesley, U.S.A, 1963.

[53] A. G. Bailey, *Electrostatic Spraying of Liquids.* Somerset, UK: Research Studies, pp. 35–39, 1988.

[54] L. Fan and C. Zhu, *Principles of Gas-Solid Flows*. 1st edition, Cambridge: Cambridge University Press, pp. 87–129, 1998.

[55] X. Ji, O. Le Bihan, O. Ramalho, C. Mandin, B. D'Anna, L. Martinon, M. Nicolas, D. Bard and J. C. Pairon, "Characterization of particles emitted by incense burning in an experimental house," *Indoor Air*, vol. 20, no. 2, pp. 147-158, 2010.

[56] G. M. Colver and S. El-Khabiry, "Modeling of DC corona discharge along an electrically conductive flat plate with gas flow", *IEEE Transactions on Industry Applications*, vol. 35, pp. 387-394, 1999.

[57] S. A. O. Ahmedou and M. Havet, "Analysis of the EHD enhancement of heat transfer in a flat duct," *IEEE Transactions on Dielectrics and Electrical Insulation*, vol. 16, no. 2, pp. 489-494, 2009.

[58] A. Shooshtari, M. Ohadi and F. H. R. Franca, "Experimental and numerical analysis of electrohydrodynamic enhancement of heat transfer in air laminar channel flow," 19th IEEE SEMI-THERM Symposium, pp. 48-52, 2003.

[59] S. Karpov and I. Krichtafovitch, "Electrohydrodynamic flow modeling using FEMLAB," presented at COMSOL multiphysics user's conference, Boston, MA, 2005.

[60] S. G. Richard, "Ion mobility measurements in a positive corona," *Journal of Applied Physics*, vol. 67, no. 6, pp. 2789-2799, 1990.

[61] J. Q. Feng, "Electrohydrodynamic flow associated with unipolar charge current due to corona discharge from a wire enclosed in a rectangular shield," *Journal of Applied Physics*, vol. 86, no. 5, pp. 2412-2418, 1999.

[62] P. C. Reist, *Aerosol Science and Technology*, 2nd edition, McGraw-Hill, 1992.

[63] J. S. Chang, A. J. Kelly and J. M. Crowley, *Handbook of Electrostatic Processes*, 1st edition, CRC Press, pp. 39-49, 1999.

[64] W. C. Hinds, *Aerosol Technology: Properties, Behavior, and Measurement of Airborne Particles*, 2nd edition, Wiley-Interscience, 1999.

APPENDIX A:

PARTICLE TRACKING CODE

```
**********************************************************************

*This program uses Range-Kutta integration scheme to solve for the seeding
*particle velocities and positions. Electric field data was imported from
*COMSOL and interpolated to particle positions using inbuilt MATLAB
*function. "xfile_june08" and "yfile_june08" in the code denotes the name of the
*field data file imported into MATLAB using "uiimport".
**********************************************************************
%Assign values to parameters
v=2;
r=(1/2)*10^-6;
% r is radius or particle
epsr=3.99;
tc=linspace(0,5*10^-3,1500);
tdel=tc(2)-tc(1);

% Universal constants;
eps=8.854187817*10^(-12);
N=10^13; % ion density
mhu=2*10^-4; % ion mobility
e=1.6*10^-19;

%2D MODEL
%X- dux=a*ux+(c1/c2)+Ex;
%Y-duy=a*uy+Ey;

c1=3.73*(v/2)*(10^-10);
c2=(-1.868*(10^-10));
% charge varied directly in INLINE equation;
% 4.21 charges for 10^8 field and t=3.3356*10^-6;
```

```
**********************************************************************
Inline function used.  All non-varying values calculated and used directly.
Reduces computational time in each time step.
**********************************************************************
duxdt=inline('((-1.8689*10^-10)/(1.23778*10^-15))*sign(ux-2)*abs(ux-
2)+Ex*qm*((1.6000e-019)/(1.23778*10^-15))','t','ux','Ex','qm');

duydt=inline('((-1.8689*10^-10)/(1.23778*10^-
15))*sign(uy)*abs(uy)+Ey*qm*((1.6000e-019)/(1.23778*10^-
15))','t','uy','Ey','qm');

n=length(tc);
charge=zeros(n);
qm=0.1; %initial charge for 1st run

%Initializing xp and yp for first 'for' loop run;xp & yp particle poistions
xp=zeros(n);
yp=zeros(n);
fx_store=zeros(n);
fy_store=zeros(n);
xp(1)=10*10^-5;
yp(1)=10*10^-5;

% Initialize y (x-velocity) and z (y velocity) array
y=zeros(n);
z=zeros(n);
% Assign initial velocity equal to that of bulk fluid
y(1)=v;
z(1)=0;

%generate meshgrid of field and positions for use in interpolation function
[xco,yco]=meshgrid(xfile_june08(13:1000,1),xfile_june08(13:1000,2));
fx=meshgrid(xfile_june08(13:1000,3),xfile_june08(13:1000,3));
fy=meshgrid(yfile_june08(13:1000,3),yfile_june08(13:1000,3));


h=tdel;

% Initial run Ex and Ey values;
Ex=interp2(xco,yco,fx,10*10^-5,10*10^-5  );
```

```
Ey=interp2(xco,yco,fy,10*10^-5,10*10^-5  );

h2=h/2;h3=h/3;h6=h/6;

*****************************************************************
Integration implementation in 'for' for positions and velocities. Field at particle
positions calculated and  used for Coulombic force and charging rate calculations
*****************************************************************

for j=2:1500

  k1x=feval(duxdt,tc(j-1),y(j-1),Ex,qm         );
  k2x=feval(duxdt,tc(j-1)+h2,y(j-1)+h2*k1x,Ex,qm  );
  k3x=feval(duxdt,tc(j-1)+h2,y(j-1)+h2*k2x,Ex,qm  );
  k4x=feval(duxdt,tc(j-1)+h,y(j-1)+h*k3x,Ex,qm    );
  y(j)=y(j-1)+h6*(k1x+k4x) + h3*(k2x+k3x)    ;
  xp(j)=xp(j-1)+0.5*(y(j)+y(j-1))*tdel;
  fx_store(j)=Ex;
  fy_store(j)=Ey;
  k1y=feval(duydt,tc(j-1),z(j-1),Ey,qm         );
  k2y=feval(duydt,tc(j-1)+h2,z(j-1)+h2*k1y,Ey,qm  );
  k3y=feval(duydt,tc(j-1)+h2,z(j-1)+h2*k2y,Ey,qm  );
  k4y=feval(duydt,tc(j-1)+h,z(j-1)+h*k3y,Ey,qm    );
  z(j)=z(j-1)+h6*(k1x+k4x) + h3*(k2x+k3x)    ;
  yp(j)=yp(j-1)+0.5*(z(j)+z(j-1))*tdel;

       Ex=interp2(xfile_june08(13:1000,1),xfile_june08(13:1000,2),fx,xp(j),yp(j),'
       spline');

       Ey=interp2(yfile_june08(13:1000,1),yfile_june08(13:1000,2),fy,xp(j),yp(j),'
       spline');

  E=sqrt(Ex^2+Ey^2);
  delcharge=(4.21/10e8)*E    ;    % charge in each time step calculated
  charge(j)=charge(j-1)+delcharge;
  qm=round(charge(j));    % rounding charge to nearest integer;

  end
```

APPENDIX B: ADDITIONAL BULK FLOW VELOCITY INFORMATION

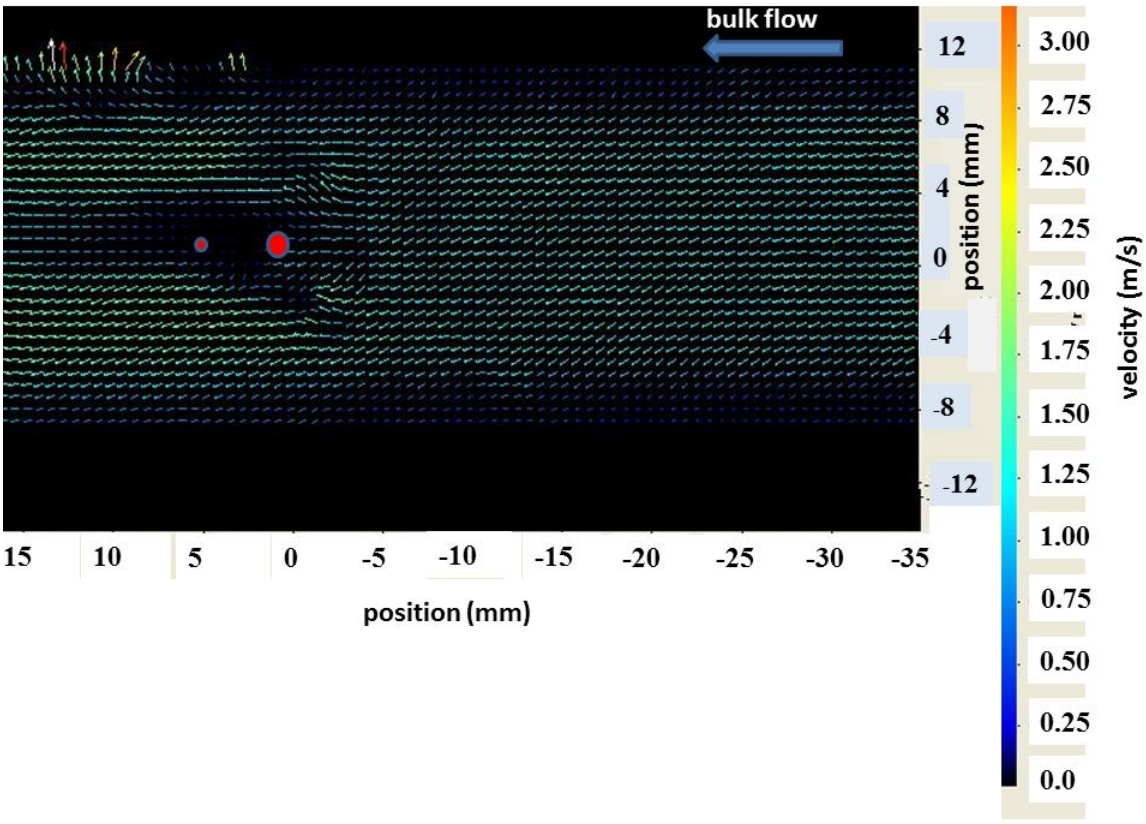

Figure B-1 Particle image velocimetry result for 1.2 m/s bulk flow without ionic wind. Collecting electrode and corona electrode are indicated by the larger and smaller red dots respectively.

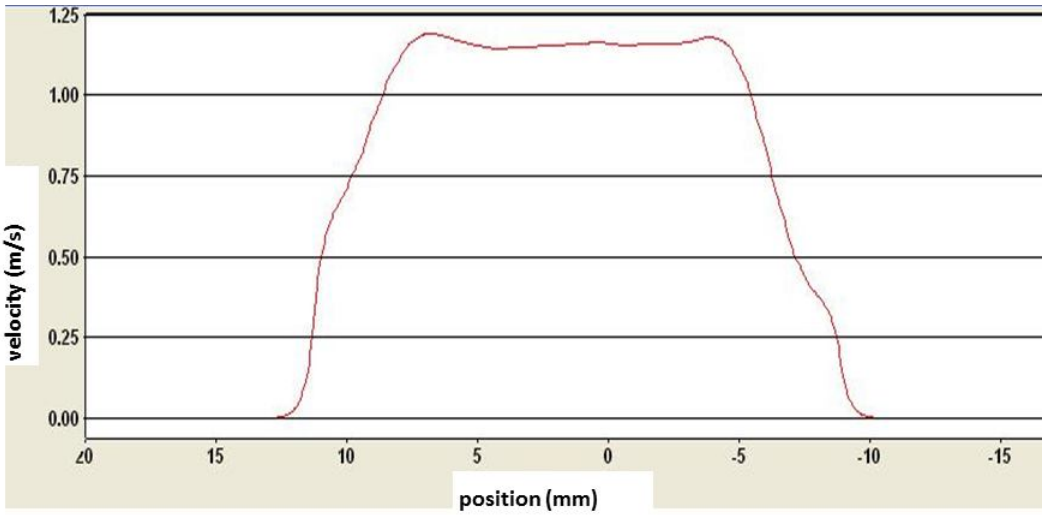

Figure B-2 Cross sectional bulk velocity for 1.2 m/s bulk flow without ionic wind.

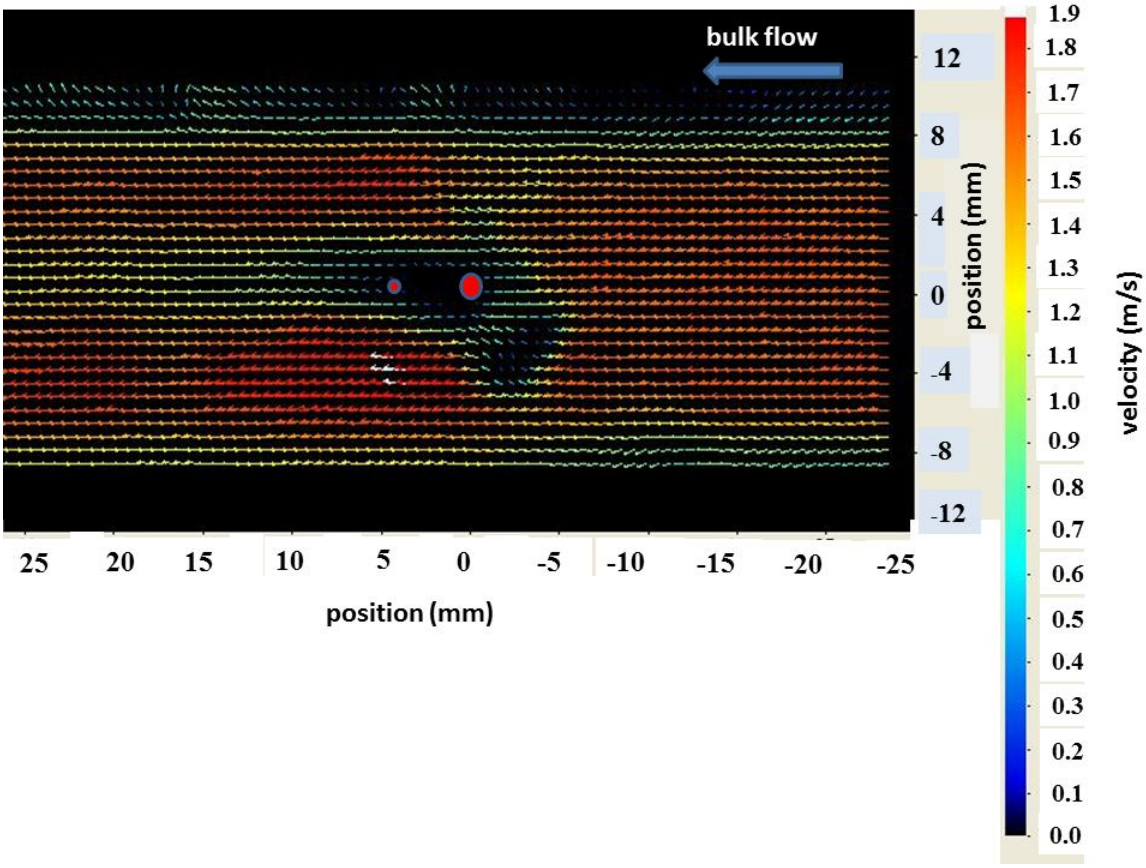

Figure B-3 Particle image velocimetry result for 1.7 m/s bulk flow without ionic wind. Collecting electrode and corona electrode are indicated by the larger and smaller red dots respectively.

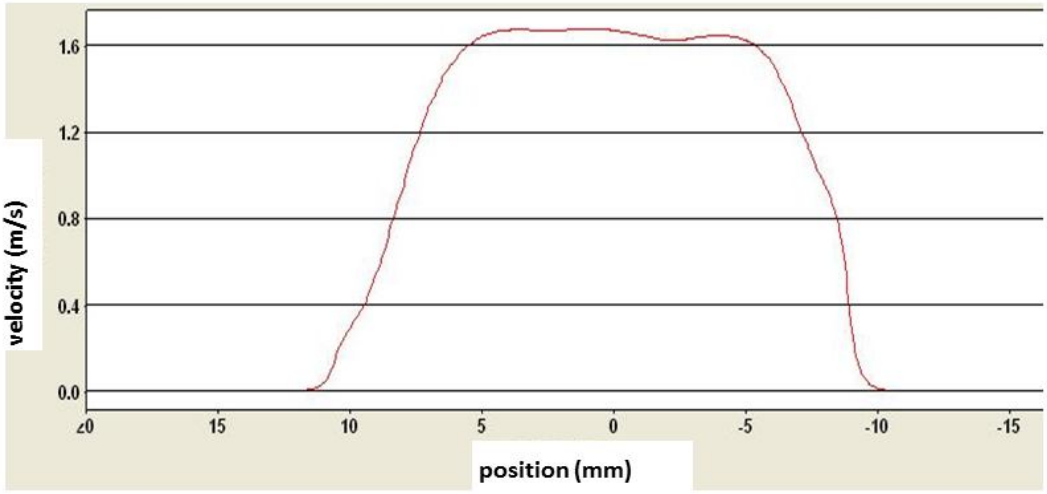

Figure B-4 Cross sectional bulk velocity for 1.7 m/s bulk flow without ionic wind.